Single deformed bubbles rising through stagnant water of surfactant concentrations beyond CMC

Yusei Iwai, Shigeo Hosokawa, Dominique Legendre, Kosuke Hayashi

International Journal of Multiphase Flow 194 (2026) 105440

Contents lists available at ScienceDirect

International Journal of Multiphase Flow

journal homepage: www.elsevier.com/locate/ijmulflow

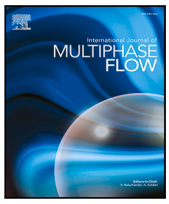

Research Paper

Single deformed bubbles rising through stagnant water of surfactant concentrations beyond CMC

Yusei Iwai [a], Shigeo Hosokawa [b], Dominique Legendre [c], Kosuke Hayashi [a,*]

[a] Graduate School of Engineering, Kobe University, 1-1 Rokkodai Nada, Kobe, 657-8501, Hyogo, Japan
[b] Graduate School of Societal Safety Science, Kansai University, 7-1 Hakubaicho, Takatsuki, 569-1116, Osaka, Japan
[c] Institut de Mécanique des Fluides de Toulouse (IMFT) - Université de Toulouse, CNRS-INPT-UPS, Allée du Professeur Camille Soula, 31400, Toulouse, France

ARTICLE INFO

Keywords:
Bubble shape
Aspect ratio
Terminal velocity
Drag force

ABSTRACT

Experiments were conducted on deformed bubbles in Triton X-100 aqueous solutions at concentrations exceeding the critical micelle concentration (CMC) to understand the bubble behavior in the so-called fully-contaminated state. The terminal velocity was significantly reduced at a concentration C of 10 mmol/m^3 (< CMC = 240 mmol/m^3), and the velocity data were in agreement with the well-known slow velocity curve for contaminated systems. However, as indicated in C beyond CMC, the terminal velocity experienced a further decrease, while the velocities at concentrations of C = 10,000 and 20,000 mmol/m^3 were the same, suggesting that at these concentrations the bubbles were completely contaminated. In the Re-Eo plane, where the Eötvös number was calculated by the effective surface tension, σ_{eq}, for the equilibrium of adsorption and desorption, the bubble Reynolds numbers of contaminated bubbles agreed with those in a higher viscosity system with the effective Morton number for σ_{eq}. Therefore, bubbles were considered to be fully covered by surfactant, which causes the surface tension reduction and the Marangoni effect. The presence of surfactant decreased the shape deformation, and the aspect ratios for C = 10,000 and 20,000 mmol/m^3 were the same, again showing that the bubbles at these concentrations were fully contaminated. The Weber number defined for σ_{eq} worked well to correlate the shapes of contaminated bubbles. A shape correlation for contaminated bubbles was developed, and an available drag correlation was extended by introducing the effects of bubble deformation to reproduce the fast and slow velocity curves of clean and contaminated bubbles that exhibit different characteristics in shape and path oscillations, in particular at C beyond CMC.

1. Introduction

Millimeter-sized bubbles in water are known to exhibit two velocity curves depending on the purity of the water; that is, bubbles in clean water draw a fast velocity curve on the velocity-diameter map as the diameter of bubble changes, while addition of surfactant (surface-active agent) to water significantly reduces the bubble terminal velocity, V_T, resulting in a slow velocity curve (Haberman and Morton, 1956; Clift et al., 1978; Peters and Els, 2012; Legendre and Zenit, 2025). The state in which a further increase in the concentration, C, of the surfactant does not affect V_T is termed the fully contaminated state (Aoyama et al., 2018), which has been considered to be reached at a concentration below the CMC (critical micelle concentration), especially for the surfactant that has a much faster adsorption rate than a desorption rate, for example Triton X-100 (Takagi and Matsumoto, 2011; Hayashi and Tomiyama, 2012). The cause of the velocity reduction is described by the immobilization of the bubble surface due to the action of Marangoni stress (Frumkin and Levich, 1947; Levich, 1962).

Surfactant monomers dissolving in the bulk liquid migrate toward the surface of a rising bubble and are adsorbed on it. They are swept by interfacial flow and accumulate in the rear part of the bubble, causing a gradient in the concentration, Γ, of the surfactant on the surface of the bubble. The presence of surfactant reduces the surface tension, and therefore the surface tension also becomes nonuniform, which induces the Marangoni stress. A large viscous stress in the liquid phase is required to balance with a large Marangoni stress, and thus, the surface velocity needs to be very small, i.e. the surface immobilization occurs. When surface advection dominates over diffusion, in other words the Péclet number is large, a large concentration gradient forms at a certain angle that separates the surface of the bubble into clean (mobile) and contaminated (immobile) regions. This model is referred to as the stagnant-cap model (Savic, 1953; Sadhal and Johnson, 1983; Cuenot et al., 1997; Palaparthi et al., 2006) and describes well the behavior of spherical bubbles. As the bulk concentration increases,

* Corresponding author.
E-mail address: hayashi@mech.kobe-u.ac.jp (K. Hayashi).

https://doi.org/10.1016/j.ijmultiphaseflow.2025.105440
Received 20 June 2025; Received in revised form 20 August 2025; Accepted 2 September 2025
Available online 10 September 2025

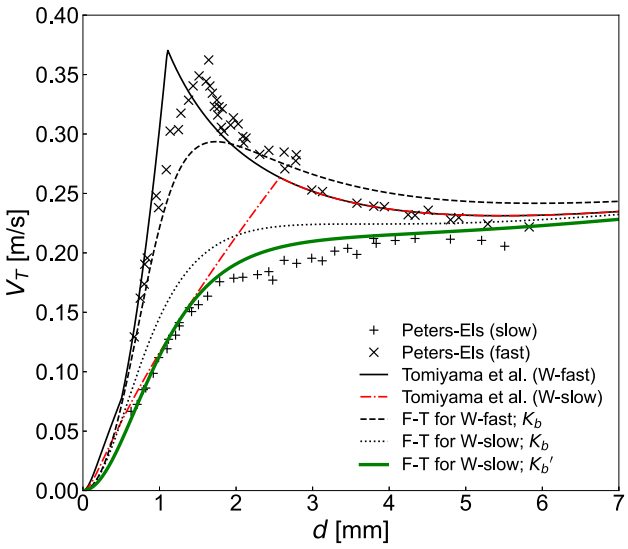

Fig. 1. Bubble terminal velocity in water. The data plots were quoted from Peters and Els (2012). Tomiyama et al.: Eqs. (3) and (5) for fast and slow curves, respectively, in water, F-T: the Fan–Tsuchiya correlation (Eq. (6)) for which K_b (Eq. (9)) with $n = 1.6$ and 0.8 are for fast and slow curves, respectively, while K_b' (Eq. (10)) with $n = 0.8$ is also used to draw slow curve. (For interpretation of the references to colour in this figure legend, the reader is referred to the web version of this article.)

the stagnant-cap angle shifts toward the bubble nose and the surface becomes totally immobile when the angle reaches the nose. When the bubble surface is entirely covered by surfactant, the mean value of the surface tension can be lower than that of the clean surface (Hayashi and Tomiyama, 2018). This change in surface tension possibly affects bubble motion, especially in the surface-tension dominant regime, in which the drag coefficient is determined by the Eötvös number (Fan and Tsuchiya, 1990; Tomiyama et al., 2002). However, studies in the literature focused mainly on the reduction of velocity by the Marangoni effect, and the role of the effective surface tension on the bubble terminal velocity and the bubble shape has not yet been discussed in detail.

The main objective of this study is to make clear the characteristics of the terminal velocity and shape of millimeter-sized bubbles in water in the fully contaminated state. Therefore, we carried out experiments on deformed bubbles in water contaminated with Triton X-100 at several concentrations lower and higher than CMC. A bubble shape and a drag correlation applicable to contaminated bubbles will be developed after the experimental data is analyzed. In Section 2, we start by briefly reviewing the characteristics of bubble velocity to introduce velocity data demonstrating the fast and slow velocity curves and correlations available in the literature and relevant dimensionless groups. The present experimental setups and methods are then described in Section 3. In the Results and Discussion section, the bubble behavior under different contamination levels is first reported in Section 4.1. The bubble velocity, the normalized bubble velocity (the bubble Reynolds number) and the drag coefficient will then be discussed in Sections 4.2 and 4.3, respectively. The dependence of the bubble aspect ratio on the contamination level will be discussed in Section 4.4 to obtain a shape correlation. In Section 4.5 a drag correlation expressed in terms of the aspect ratio will be proposed. Discussion on the bubble behavior in high surfactant concentrations will be given in the end of Section 4.

2. Brief review on bubble terminal velocity and introduction of relevant dimensionless groups

We briefly review available bubble velocity correlations and introduce some important dimensionless groups relevant to the terminal velocity in this section. Fig. 1 demonstrates the relationship between V_T and d of bubbles in water by making use of the velocity data reported by Peters and Els (2012), which cover the range of d from 0.5 mm to 6 mm, to observe the entire picture of the velocity characteristics. Peters and Els (2012) obtained the fast and slow velocity data by producing single bubbles by quickly and slowly pushing them, respectively, into tap water. They concluded that the bifurcation of the velocity data is attributed to initial surface contamination. All bubbles were classified into either the fast (the cross symbols in the figure) or the slow regime (the plus symbols), and they did not observe bubbles in intermediate states. On the other hand, Tagawa et al. (2014) observed the intermediate states depending on the concentration of surfactant and reported the bubble path map described by the normalized drag (Cuenot et al., 1997) and the bubble Reynolds number. Furthermore, some researchers reported that clean bubbles can also take intermediate states and the velocity data lie within the range in-between the fast and slow regimes (Wu and Gharib, 2002; Okawa et al., 2003; Tomiyama, 2004; Hosen et al., 2024); the scattering in the bubble velocity was attributed to various bubble shapes depending on the ratio of bubble size to injection nozzle size, in other words, initial shape deformation. The cause of velocity scattering is still an open question, and we do not discuss this point further here. For the fast velocity data of Peters and Els (2012), the bubble velocity of small bubbles increases with d, while the velocity reduction takes place for the intermediate bubble size. Then the bubble velocity increases again with d.

The dependence of V_T in the fast velocity regime on d can be understood from the following order of magnitude analysis. In the terminal state of a bubble in still liquid, the local stress balance along the normal to bubble surface yields $c_i F_i + c_\mu F_\mu - c_b F_b - c_\sigma F_\sigma \sim 0$ as a first-order expression (Tomiyama and Hayashi, 2018; Legendre and Zenit, 2025), where $c_i, c_\mu, c_b, c_\sigma$ are constants, $F_i = \rho_L V_T^2 d^2$, $F_\mu = \mu_L V_T d$, $F_b = \Delta\rho g d^3$, $F_\sigma = \sigma d$, ρ_L is the liquid density, μ_L is the liquid viscosity, $\Delta\rho$ is the density difference between the two phases, σ is the surface tension, and g is the magnitude of gravity acceleration (see Appendix C for the details). Considering the limiting case of $d \to 0$, we have $V_T \to 0$. Because of the strong action of surface tension, the bubble maintain spherical shape (Clift et al., 1978). The distribution of surface tension force acting on the spherical surface is symmetric, so that the surface-tension contributions at the bubble nose and equator cancel out each other when the difference between these contributions is taken. Thus, for tiny bubbles, the surface tension force acts to keep their shapes spherical, but plays no role in the rise velocity. In addition, $F_i \ll F_\mu, F_b$, so that the balance equation reduces to $c_\mu F_\mu - c_b F_b \sim 0$. Thus, $V_T \sim (c_b/c_\mu)(\Delta\rho g d^2/\mu_L)$ ($\propto d^2$). In dimensionless form, $Re \sim (c_b/c_\mu) Ar^2$, where the bubble Reynolds number and Archimedes number are, respectively, defined by

$$Re = \frac{\rho_L V_T d}{\mu_L} \tag{1}$$

and $Ar = \sqrt{\rho_L \Delta\rho g d^3}/\mu_L$. Bubbles of intermediate sizes cannot maintain spherical shape and their shapes may be either ellipsoidal or distorted ellipsoidal. Assuming that the bubble shape results from the balance between the dynamic pressure and surface tension (Moore, 1965) yields $c_i F_i - c_\sigma F_\sigma \sim 0$, and therefore $V_T \sim (c_\sigma/c_i)^{1/2}\sqrt{\sigma/\rho_L d}$ ($\propto d^{-1/2}$). Nondimensionalizing this equation yields $We \sim c_\sigma/c_i$, where the Weber number is defined by

$$We = \frac{\rho_L V_T^2 d}{\sigma_0} \tag{2}$$

based on the surface tension, σ_0, of surfactant-free surface. The shape of a large bubble is no longer neither spherical nor ellipsoidal, but a slice of a sphere called spherical-cap. Because of its large size, the inertial and buoyant forces are dominant rather than the viscous and surface tension forces. Therefore, $c_i F_i - c_b F_b \sim 0$, which results in $V_T \sim (c_b/c_i)^{1/2}\sqrt{\Delta\rho g d/\rho_L}$ ($\propto d^{1/2}$) and $Fr \sim (c_b/c_i)^{1/2}$ (Davies and Taylor, 1950), and Fr is the Froude number defined by $Fr = V_T/\sqrt{\Delta\rho g d/\rho_L}$.

Combining the latter two gives $V_T \sim \sqrt{(c_\sigma/c_i)\sigma/\rho_L d + (c_b/c_i)\Delta\rho g d/\rho_L}$ or, equivalently, $We \sim (c_\sigma/c_i) + (c_b/c_i)Eo$. The fast velocity data of Peters and Els (2012) pretty agrees with the following correlation proposed by Tomiyama et al. (1998):

$$C_D = \max\left\{\min\left[\frac{16}{Re}\left(1+0.15Re^{0.687}\right), \frac{48}{Re}\right], \frac{8}{3}\frac{Eo}{Eo+4}\right\} \tag{3}$$

which consists of the Hadamard–Rybczynski solution ($c_\mu/c_b = 12$) (Hadamard, 1911; Rybczynski, 1911) with inertial correction (Schiller and Naumann, 1933), the Levich drag for spherical bubble in high Reynolds number limit ($c_\mu/c_b = 36$) (Levich, 1962), and the Mendelson drag ($c_\sigma/c_i = 2$ and $c_b/c_i = 1/2$) (Mendelson, 1967; Tomiyama et al., 1998) based on wave analogy; these drag coefficients correspond to the velocity expressions described above for the given values of the coefficients. The Eötvös number, Eo, is defined by

$$Eo = \frac{\Delta\rho g d^2}{\sigma_0} \tag{4}$$

The plus symbols in the figure show Peters' velocity data of slow bubbles. These bubbles are much slower than those of fast velocity, especially small bubble sizes. For fully-contaminated systems, Tomiyama et al. (1998) proposed the following correlation:

$$C_D = \max\left\{\frac{24}{Re}\left(1+0.15Re^{0.687}\right), \frac{8}{3}\frac{Eo}{Eo+4}\right\} \tag{5}$$

This correlation (the dash-dotted line) agrees with Peters' data for $d < 1.2$ mm, while, for larger bubbles, the correlation largely deviates from the slow velocity curve, clearly showing that the drag correlation, $C_D = 8Eo/3(Eo+4)$, needs to be modified to express the slow velocity curve.

Fan and Tsuchiya (1990) proposed to combine two correlations for small and large bubbles:

$$V_T = \left(V_{T1}^{-n} + V_{T2}^{-n}\right)^{-1/n} \tag{6}$$

$$V_{T1} = \frac{\Delta\rho g d^2}{K_b \mu_L} \tag{7}$$

$$V_{T2} = \sqrt{\frac{2c\sigma}{\rho_L d} + \frac{\Delta\rho g d}{2\rho_L}} \tag{8}$$

where $c = 1.2$, $n = 1.6$ and 0.8 for clean (fast velocity curve) and contaminated (slow velocity curve) cases, respectively. K_b is given by

$$K_b = \max\left[14.7Mo^{-0.038}, 12\right] \tag{9}$$

Fig. 1 shows that although this correlation reproduces the trend of the fast velocity data for $d \geq 2$ mm, the slow velocity data are largely overestimated at the small and intermediate bubble sizes. Fan and Tsuchiya (1990) recommended $K_b = 37$ given by Eq. (9) both for fast and slow bubbles. This value is, however, comparable to the Levich drag ($K_b\ (= c_\mu/c_b) = 36$; $C_D = 48/Re$) for clean spherical bubbles and may not be appropriate for contaminated bubbles. Therefore, for the slow velocity curve, we take

$$K_b' = 3K_b/2 \tag{10}$$

instead of the original K_b. Taking this value means $C_D = 72/Re$, which was employed for slightly contaminated systems by Tomiyama et al. (1998). This change in the coefficient gives a better expression for the slow velocity curve as shown in Fig. 1 (the thick curve in green color). We will use the Fan–Tsuchiya correlation for drawing the drag and Reynolds number curves corresponding to the fast and slow velocity regimes in Section 4.3 for reference. A drag correlation accounting for the shape effect based on the present data will be presented in Section 4.5.

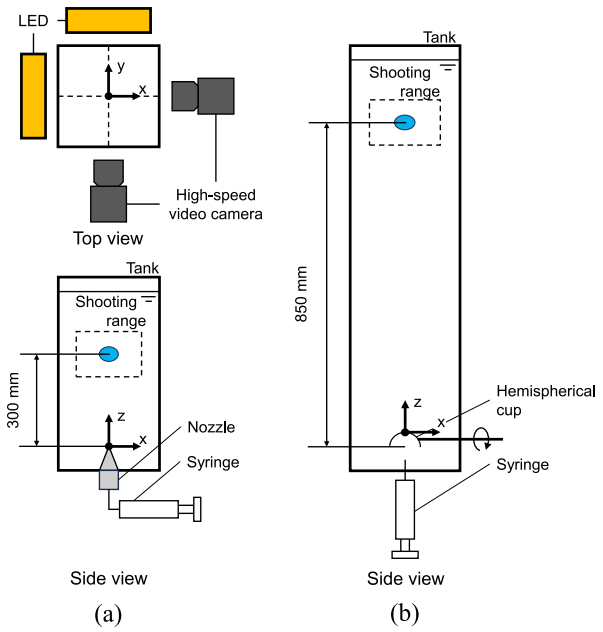

Fig. 2. Experimental setups: (a) equipment for contaminated bubble experiments; (b) equipment for clean bubble experiments.

3. Experimental method

3.1. Experimental apparatus and method

Air bubbles were produced using a nozzle (Ikeuchi, standard straight nozzle, CP series) installed at the bottom of an 150 × 150 × 500 mm tank filled with contaminated water or a contaminated glycerol-water solution, as shown in Fig. 2(a). The interval between two runs was set to over 30 s to ensure the stagnant liquid condition (Haberman and Morton, 1956; Takagi et al., 2008). The terminal velocity and the aspect ratio of a bubble were calculated from images obtained at 300 mm above the tip of the nozzle by using high-speed video cameras (Integrated Design Tool, M3, 520 fps) from two orthogonal directions. The experiments were carried out at atmospheric pressure and room temperature (25 ± 0.5 °C).

We also carried out measurements for clean cases to obtain reference data by using purified water and a glycerol-water solution. In these cases, a hemispherical cup installed at the bottom of a 200 × 200 × 1300 mm tank (Fig. 2(b)) was used to generate single bubbles (Landel et al., 2008; Hosoda et al., 2014; Ruth et al., 2022). Air was injected from a syringe into the hemispherical cup. When multiple bubbles were present in the cup, they were merged in the cup to produce single bubble. Then, the single bubble was released into the liquid phase by rotating the cup 180 degrees. The bubble images were captured at 850 mm above the hemispherical cup. We used the larger tank than in the contaminated bubble case since the amplitude of oscillation and the rise velocity of clean bubbles are typically larger than those of contaminated bubbles; for example, a clean bubble of $d = 1.5$ mm exhibits a five times larger oscillation amplitude and twice larger rise velocity as shown later in Figs. 9 and 10, respectively.

3.2. Water case

The liquid phase was purified water (Merck, Elix Essential UV5) and water contaminated with Triton X-100, which is soluble in water and has often been used in literature (Bel Fdhila and Duineveld, 1996; Zhang and Finch, 2001; Takagi and Matsumoto, 2011; Tagawa et al., 2014; Hosokawa et al., 2017; Mori et al., 2024; Igarashi et al., 2025) for

studying bubble dynamics in contaminated system. The concentrations, C, of Triton X-100 were 10, 250, 10,000 and 20,000 mmol/m^3. The fluid properties of the liquids are given in Table 1. The liquid densities were measured using a specific gravity meter (Ando Instrument, JIS B7525). The liquid viscosities were estimated from measured data given by Kushner and Hubbard (1954); the estimated values show that the increase in viscosity is at most 5.6% even with the highest concentration of surfactants. The Morton number

$$Mo = \frac{\mu_L^4 \Delta\rho g}{\rho_L^2 \sigma_0^3} \tag{11}$$

in the case of clean water is $\log Mo = -10.8$.

In contaminated systems, the surface tension at the bubble surface is reduced as a result of adsorption of the surfactant. In the absence of fluid flow, the surface tension, σ_{eq}, in the equilibrium of adsorption and desorption of the surfactant is given by the following isotherm (Chang and Franses, 1995):

$$\sigma_{eq} = \max\left[\sigma_0 - RT\Gamma_{max} \ln\left(1 + \frac{C}{a}\right), \sigma_\infty\right] \tag{12}$$

where R is the gas constant, T is the temperature, Γ_{max} is the saturation concentration, a is the ratio of the desorption rate to the adsorption rate, and σ_∞ is the minimum value of surface tension when the interfacial surfactant concentration is close to Γ_{max} (Olgac and Muradoglu, 2013; Legendre and Zenit, 2025). It should be noted that, for $C >$ CMC, the surfactant forms micelles in the liquid phase, and the micelles are no longer active in migrating to the surface due to its stability. Therefore, $\sigma_\infty = \sigma_{CMC}$ for static interface. Kurimoto et al. (2013) assumed $\sigma_\infty = \sigma_{CMC}$ (the surface tension for the bulk concentrations above CMC) in their numerical simulations of contaminated drops moving in liquids. For Triton X-100 in water, $a = 6.7 \times 10^{-4}$ mol/m^3, $\Gamma_{max} = 2.9 \times 10^{-6}$ mol/m^2, CMC = 240 mmol/m^3, and $\sigma_{CMC} = 30$ mN/m (Mori et al., 2024). Therefore, the normalized concentrations, C/CMC, in the present conditions are 0.04, 1.0, 42, and 83 for C = 10, 250, 10,000 and 20,000 mmol/m^3, respectively, and their Langmuir numbers, La, are 15, 373, 15,000 and 30,000, where La is defined by

$$La = \frac{C}{a} \tag{13}$$

$La \gg 1$ means that the adsorption is dominant. The equilibrium value Γ_{eq} of the interfacial surfactant concentration Γ for C is given by

$$\Gamma_{eq} = La(1 + La)^{-1} \tag{14}$$

Since $\sigma_{eq} = \sigma_0$ when $C = 0$, let us define the (effective) Morton number as

$$Mo_{eq} = \frac{\mu_L^4 \Delta\rho g}{\rho_L^2 \sigma_{eq}^3} \tag{15}$$

Zhang and Finch (2001) pointed out that the travel distance required to reach the adsorption–desorption equilibrium can be long, especially for low concentrations of surfactants. According to their results (Fig. 2 in their paper), the setup elevation of 300 mm to observe bubble motion is high enough for $C \geq 10$ mmol/m^3.

3.3. Glycerol-water solution case

As shown in Table 1, $\log Mo_{eq}$ in the water case increases from −10.8 to −9.6 as C increases up to CMC or higher. The force balance between the drag and buoyancy (Eq. (21)) is written in dimensionless form as

$$Re = \sqrt{\frac{4}{3C_D}} \left[\frac{Eo^3}{Mo}\right]^{1/4} \tag{16}$$

By assuming that, for millimeter-sized bubbles in water, C_D is a function of Eo (Eq. (3)) and Eo is small enough to have $C_D \propto Eo$ (Tomiyama et al., 1998), one can write $Re \propto (Eo/Mo)^{1/4}$ from the force balance (Legendre and Zenit, 2025). As can be clearly seen in this scaling, the surface tension plays a role in the normalized bubble velocity (Re) via the dimensionless groups, Eo and Mo. It would be worth comparing bubble data of Mo corresponding to those of contaminated ones to discuss the effects of surfactant on the surface property in the bubble behavior. Therefore, we carried out the experiments with a clean glycerol-water solution having Mo same as Mo_{eq} of the contaminated water, and the glycerol data will be used for comparison on the dimensionless maps, i.e. the C_D-Re and Re-Eo maps in Section 4.3. The glycerol concentration was 23.6 wt% to realize $\log Mo = -9.6$ (see the table for the fluid properties). A glycerol solution with Triton X-100 of $C = 10$ mmol/m^3 was also used, for which the effective Morton number was −9.1 due to the reduction in surface tension. The values of σ in the cases of glycerol solution were measured using the pendant bubble method (see Appendix A) (Misak, 1968; Pan et al., 1998; Mori et al., 2024).

Table 1
Physical properties of each solution. W: water, GW: glycerol-water solution of 23.6 wt%, TX: Triton X-100. The value attached to TX indicates the surfactant concentration in unit [mmol/m^3]. The Morton numbers are calculated using Eqs. (11) and (15) for clean and contaminated cases, respectively.

	ρ_L [kg/m^3]	μ_L [mPa s]	σ [mN/m]	Mo	$\log Mo$
W (Clean)	997.1	0.89	$\sigma_0 = 73$	1.7×10^{-11}	−10.8
W + TX10	997.3	0.89	$\sigma_{eq} = 52$	4.4×10^{-11}	−10.4
W + TX250	997.3	0.89	30	2.3×10^{-10}	−9.6
W + TX10000	997.3	0.92	30	2.6×10^{-10}	−9.6
W + TX20000	997.8	0.94	30	2.9×10^{-10}	−9.5
GW (Clean)	1054	1.73	$\sigma_0 = 72$	2.3×10^{-10}	−9.6
GW + TX10	1055	1.73	$\sigma_{eq} = 47$	8.0×10^{-10}	−9.1

3.4. Image processing

A background subtraction was applied to the front and side images of a bubble obtained by the two high-speed video cameras (Fig. 3(a)). The discriminant analysis method was then used to determine the threshold value for binarization (Otsu, 1979). The bubble shape was obtained by binarizing the images (Fig. 3(b)). The bubble shape was reconstructed from the stereoscopic images by assuming that the horizontal cross-sectional shape of the bubble was elliptical (Fig. 3(c)) (Hosoda et al., 2014). Piling the elliptic disks of thickness δ (1 pix) up in the vertical direction yields an approximated three-dimensional bubble shape as shown in Fig. 3(d). As shown in the figure, the major and minor axes of the ellipse are L_{Fj} and L_{Sj}, respectively, and the subscript j denotes the index of the pixel in the vertical direction. The bubble volume, ϑ_B, was therefore calculated as

$$\vartheta_B = \sum_{j=1}^{N} \frac{\pi L_{Fj} L_{Sj} \delta}{4} \tag{17}$$

where N is the total number of the vertically stacked elliptic disks. The sphere-volume-equivalent bubble diameter, d, was then obtained as

$$d = \left[\frac{6\vartheta_B}{\pi}\right]^{1/3} \tag{18}$$

The vertical coordinate, z_B, of the center of gravity was calculated by

$$z_B = \vartheta_B^{-1} \sum_{j=1}^{N} \frac{\pi L_{Fj} L_{Sj} \delta}{4} z_j \tag{19}$$

where z_j is the center position of the jth disk. Note that for oscillating bubbles, the length scale of the bubble in the image slightly changes as the bubble moves in the depth direction. Therefore, scale adjustments were made for each instantaneous image based on the bubble position (see Appendix B).

The instantaneous rise velocity, $V(t)$, of the bubble was calculated as

$$V(t) = \frac{z_B(t) - z_B(t - \Delta t)}{\Delta t} \tag{20}$$

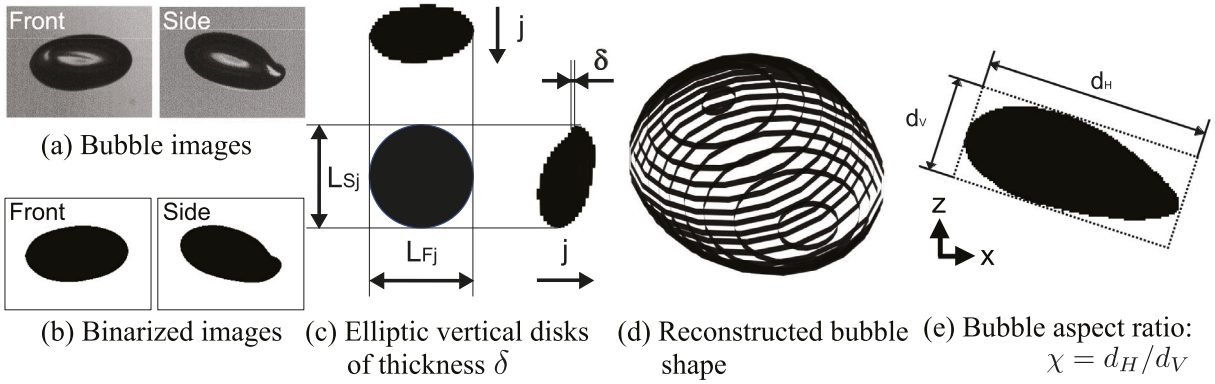

Fig. 3. Bubble reconstruction process ((a)–(d)) and evaluation of bubble aspect ratio (e).

where t is the time and Δt is the time duration between two successive images. Then V_T was calculated as the time-averaged value of $V(t)$. The drag coefficient, C_D, was calculated from the force balance between the drag and the net buoyancy:

$$C_D \frac{\rho_L V_T^2}{2} \frac{\pi d^2}{4} = \Delta\rho g \vartheta_B \tag{21}$$

Bubble images were taken with the constant spatial resolution, so that the measurement error in d tended to be large for small bubbles. The uncertainty in d at 95% confidence interval was at most 8.8%. The error in terminal velocity estimated from the spatial resolution and the traveling time was 1.86 mm/s at the largest.

The bubble aspect ratio is defined by

$$\chi = \frac{d_H}{d_V} \tag{22}$$

where d_H and d_V are the major and minor axes, which were detected by fitting a square to the binarized bubble image as shown in Fig. 3(e) (Aoyama et al., 2016); its uncertainty was less than 3.5%. The aspect ratios were calculated for both front and side images and the mean value of them will be shown as χ in the following sections.

4. Results and discussion

4.1. Bubble shape and path

Typical bubble shapes and paths observed in the water cases are shown in this section. Fig. 4 shows bubbles of $d \sim 2$ mm. In the case of clean water ((a)), the bubble exhibits a spiral path with a large amplitude of oscillation. The bubble shape is ellipsoidal, and the deviation from the spherical shape is large. Adding 10 mmol/m^3 of surfactant ((b)) drastically changes the trajectory and shape of the bubble. The bubble path in this case is zigzag with a much smaller amplitude of oscillation, and the shape deformation is mitigated. The contaminated bubbles are slower than the clean one. The bubble shape at $C = 250$ mmol/m^3 is similar to that of $C = 10$ mmol/m^3; they are much rounder than the clean bubble. The rise velocity is somewhat reduced compared to the case of (b). This bubble of $C = 250$ mmol/m^3 and those of 10,000 and 20,000 mmol/m^3 are on zigzagging paths. Substantial differences in motion, shape, and velocity are not found between (d) and (e), implying the saturation of the surfactant effects on the bubble rise motion.

Bubbles around $d = 3$ mm are shown in Fig. 5. The clean bubble of this size ((a)) is more deformed compared to that of $d = 2$ mm. However, the rise path is zigzagging, unlike the 2 mm bubble. A relation between the transition from spiral to zigzagging path and the Weber number will be discussed in Section 4.4. The shape deformation is more remarkable, and the bubble shape does not have fore-aft symmetry. The presence of surfactant again drastically changes the bubble shape; the contaminated bubbles of 3 mm are deformed spheroidal ((b)–(e)). Their paths are zigzagging as in the cases of 2 mm contaminated bubbles. The addition of surfactant also reduces the rise velocity, while the reduction effect at very high surfactant concentrations is no longer clearly visible. The velocity data will be given in the next section and a detailed discussion of the effects of surfactant on the velocity will be given there.

Fig. 6 shows bubbles around $d = 4$ mm. The clean bubble ((a)) shows not only a path oscillation but also a shape oscillation as especially seen in the side image. The rise path exhibits irregular fluctuations due to the shape oscillation; therefore, the path is termed distorted. The contaminated bubbles shown in Fig. 6(b)–(d) are also on zigzagging paths with some shape oscillations. Compared to the case of $C = 10$ mmol/m^3, the more contaminated bubbles exhibit higher aspect ratios (larger deformation). A similar trend can be found in the cases of 2 and 3 mm; however, it becomes more observable at $d = 4$ mm due to greater shape deformation. For a clean bubble of 5 mm, variations in its shape are more pronounced, as shown in Fig. 7(a). The significant deformation is caused by the inertial force being greater than the surface tension force, resulting in the bubble's edge often forming a sharp shape. This is then followed by a rapid lateral pulling motion driven by a strong surface tension force acting on that large curvature bubble edge. The bubble path can be classified as zigzagging; however, the complex oscillating motion is close to the so-called wobbling regime. The shape oscillation with surfactant of $C = 10$ mmol/m^3 shown in Fig. 7(b) is much weaker compared to the case of clean bubbles. However, at the larger surfactant concentrations ((c)–(d)), the bubble shape shows somewhat irregular shape fluctuations, unlike the smaller bubbles.

The effects of the surfactant on the oscillating motion of the bubbles is evaluated in a quantitative manner, that is, the amplitude, s, of oscillating motion was calculated using the following equation:

$$s = \sqrt{\Delta x^2 + \Delta y^2} = \sqrt{(x_{max} - x_{min})^2 + (y_{max} - y_{min})^2} \tag{23}$$

where x_{max} and x_{min} are the maximum and minimum coordinates of a bubble in the x direction, respectively, same in the y direction as well, as shown in Fig. 8. It should be noted that s is not exactly the amplitude and should be regarded as its indicator. Since bubble paths could be distorted, in particular for bubbles of large size, and the amplitude of such path cannot be clearly defined, we used the amplitude indicator defined in the above fashion. Fig. 9 shows the relationship between χ and s/d. Two distinct trends can be observed; in the clean case, s/d is large when the shape deformation is moderate and has a proportional relationship with χ, which can be expressed as

$$\frac{s}{d} = \frac{2.2 - \chi}{0.05} \tag{24}$$

The order of s/d in the clean system is comparable with that reported in Riboux et al. (2010) (the green square symbols), who measured the oscillation amplitude of single bubbles in filtered tap water for $d = 1.6 \sim 2.5$ mm. On the other hand, the contaminated data exhibit

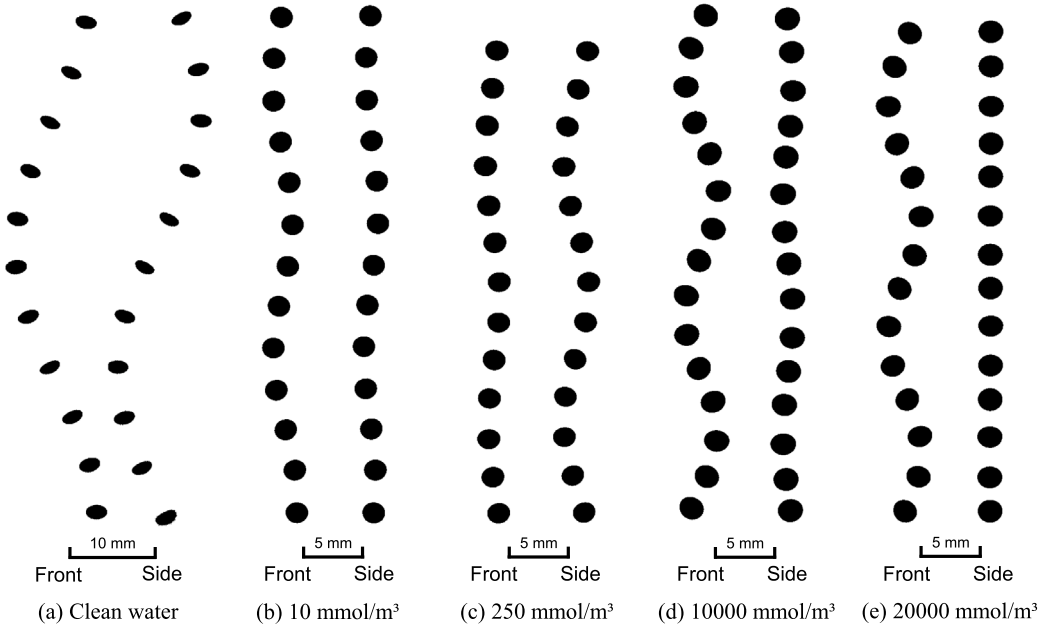

Fig. 4. Motion of bubbles in water. (a) d = 2.00 mm, χ = 1.66 (spiral), (b) 1.82 mm, 1.08 (c) 1.83 mm, 1.13 (d) 2.01 mm, 1.12 (e) 1.96 mm, 1.13 ((b)–(e): zigzagging). The time interval, Δt_{img}, between sequential images is 0.019 s.

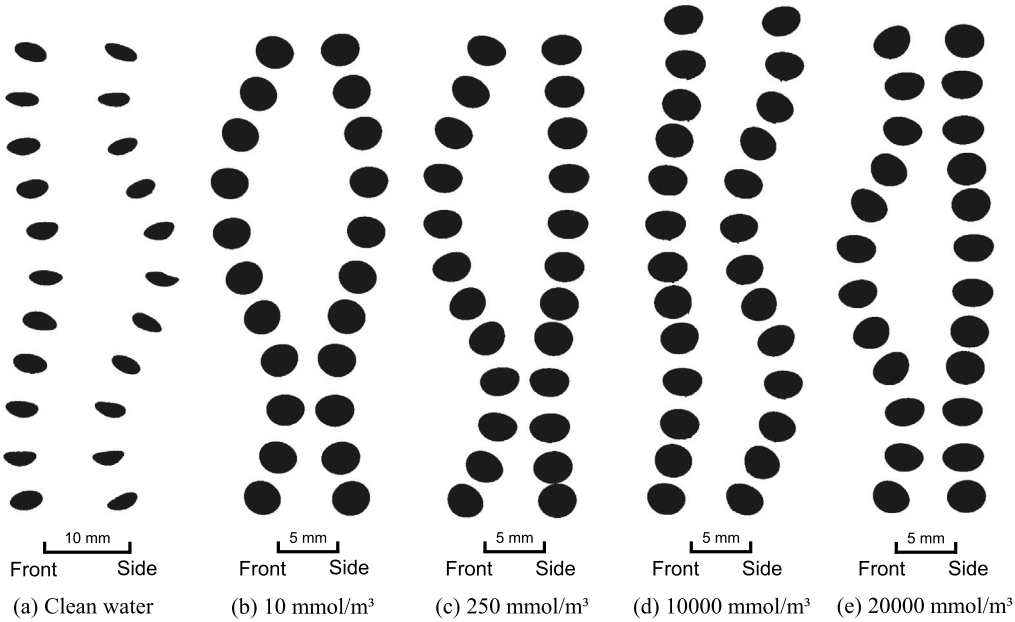

Fig. 5. Motion of bubbles in water. (a) d = 3.00 mm, χ = 1.98 (b) 3.01 mm, 1.16 (c) 2.99 mm, 1.28 (d) 2.98 mm, 1.24 (e) 3.00 mm, 1.30 ((a)–(e): zigzagging). Δt_{img} = 0.019 s.

almost constant values around 2 for $1.2 \leq \chi \leq 1.5$ (the dotted line). For C = 10 and 250 mmol/m^3, the s/d values are somewhat larger than 2, while the data of C = 10,000 and 20,000 mmol/m^3 are overlapped at about 2. With larger values of χ, s/d shows a slightly decreasing trend approximated by

$$\frac{s}{d} = \frac{2.2 - \chi}{0.35} \tag{25}$$

The oscillation of the clean bubbles is greater than that of the contaminated bubbles. Therefore, in the case of a contaminated bubble, the bubble is not easily oscillated and deformed, demonstrating the impact of surface contamination on the bubble oscillation. The tight relationships between χ and s is a consequence of the wake/path instability of a deformed bubble (Magnaudet and Mougin, 2007; Bonnefis et al., 2024), and the fact that the above empirical equations converge to $s/d = 0$ at χ = 2.2 implies that the contamination effect mitigates as the bubble size increases, in other words the inertial effect becomes dominant rather than the capillary force. We will discuss how the bubble velocity changes with different concentrations of surfactant in the next section, and a relation between the aspect ratio and relevant dimensionless groups will be given in Section 4.4.

4.2. Terminal velocity

Fig. 10 shows the velocity data obtained in the present experiments with clean and contaminated water in comparison with the velocity

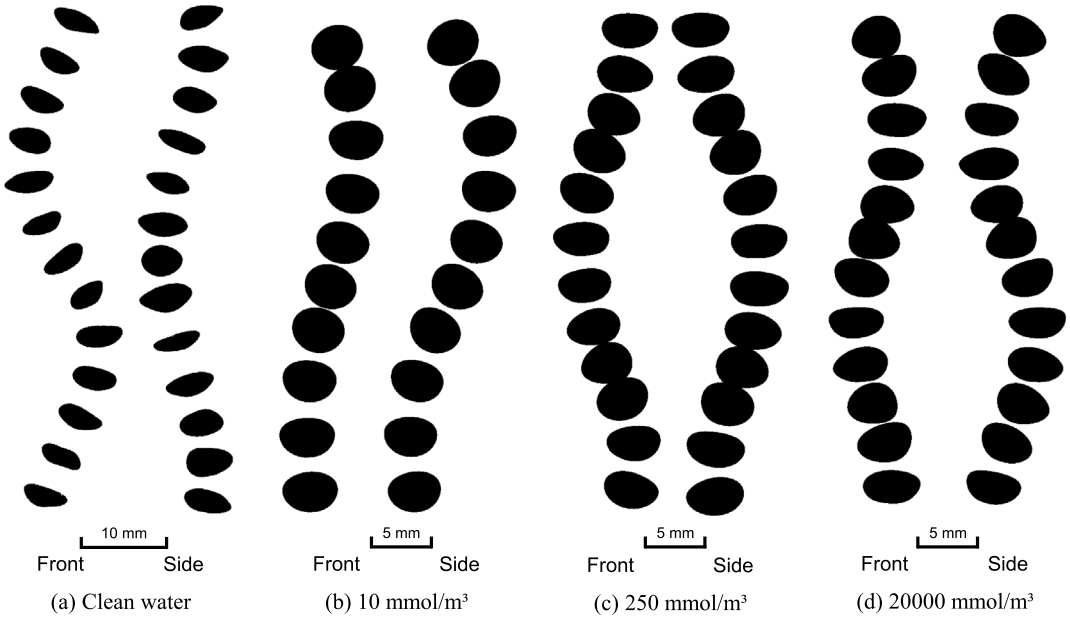

Fig. 6. Motion of bubbles in water. (a) d = 4.02 mm χ = 1.95 (distorted), (b) 4.06 mm, 1.24 (c) 4.02 mm, 1.43 (d) 3.99 mm, 1.44 ((b)–(d): zigzagging). Δt_{img} = 0.019 s.

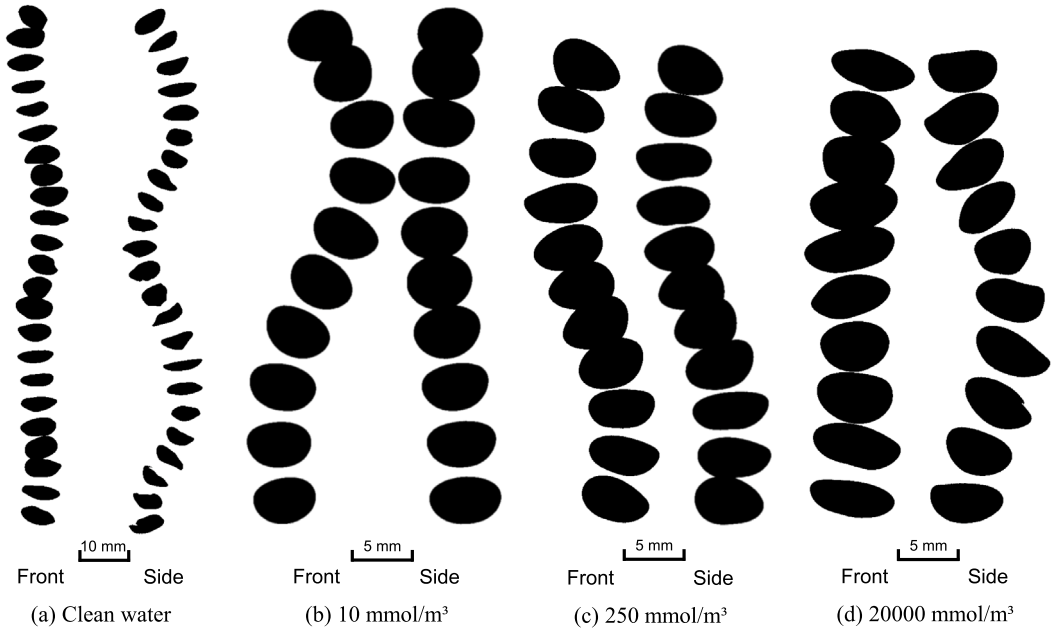

Fig. 7. Motion of bubbles in water. (a) d = 4.99 mm, χ = 2.01 (distorted), (b) 5.01 mm, 1.34 (c) 5.00 mm, 1.55 (d) 5.04 mm, 1.69 ((b)–(d): zigzagging). Δt_{img} = 0.019 s.

correlations introduced in Section 2. The clean water data agree with the fast velocity data reported by Peters and Els (2012) although the data exhibit some dispersion, as also observed in the literature (Okawa et al., 2003; Hosen et al., 2024). Although the Fan–Tsuchiya correlation tends to somewhat overestimate V_T for $d > 4$ mm, the agreement between the present data and the correlation is reasonable.

The present data show that the addition of C = 10 mmol/m^3 of surfactant mitigates the scattering of the data and V_T is much lower than that of the fast velocity curve. The velocity data are comparable to the slow velocity data of Peters and Els (2012). However, the further increase in C up to C = 250 mmol/m^3 (≈CMC) induces a reduction in V_T, while V_T does not change much for C above CMC even with the notable increase in C, i.e. 10,000 and 20,000 mmol/m^3. The good agreement between the data of C = 10,000 and 20,000 shows that the effects of the surfactant on V_T are saturated and that the bubbles are fully contaminated in these concentrations from a point of view of V_T. Importantly, the velocity data in the fully contaminated state is lower than the slow velocity evolution reported by Peters and Els (2012) and that of C = 10 mmol/m^3.

4.3. Bubble Reynolds number and drag coefficient

Fig. 11 shows the drag coefficients plotted against the bubble Reynolds number. Note that the difference between the drag data of Peters' and our fast velocity data is mainly due to the different water temperature (20 °C in the former experiment), resulting in $\log Mo$ =

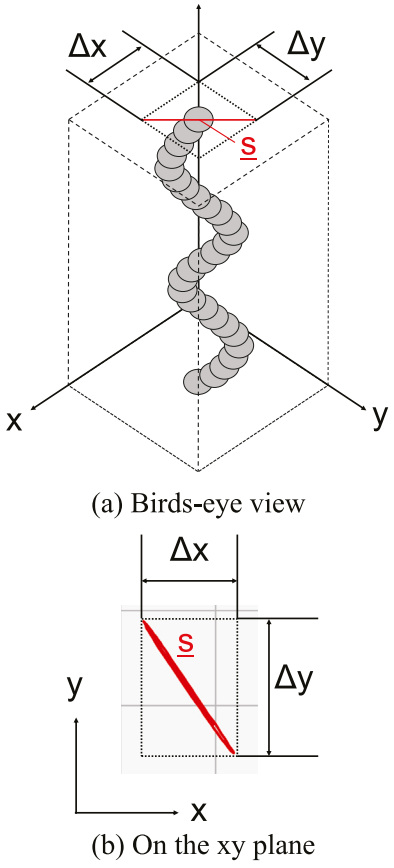

Fig. 8. Indicator s of amplitude of path oscillation. (a) definition of s, (b) example of s for zigzagging path (contaminated bubble of d = 2.62 mm at C = 20,000 mmol/m^3)).

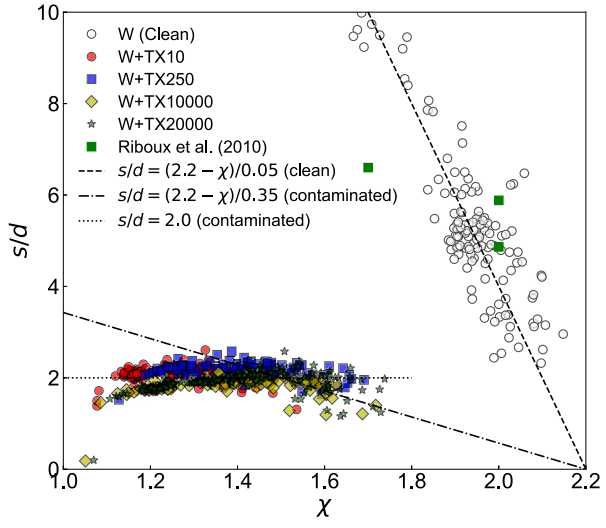

Fig. 9. s/d as function of bubble aspect ratio. The green squares are for Riboux et al. (2010); they measured the oscillation amplitude, A, of single bubbles in filtered tap water and those bubbles exhibited spiral motion rather than zigzagging, and therefore s values for their data were estimated by setting $x_{max} - x_{min} = y_{max} - y_{min} = 2A$ in Eq. (23). (For interpretation of the references to colour in this figure legend, the reader is referred to the web version of this article.)

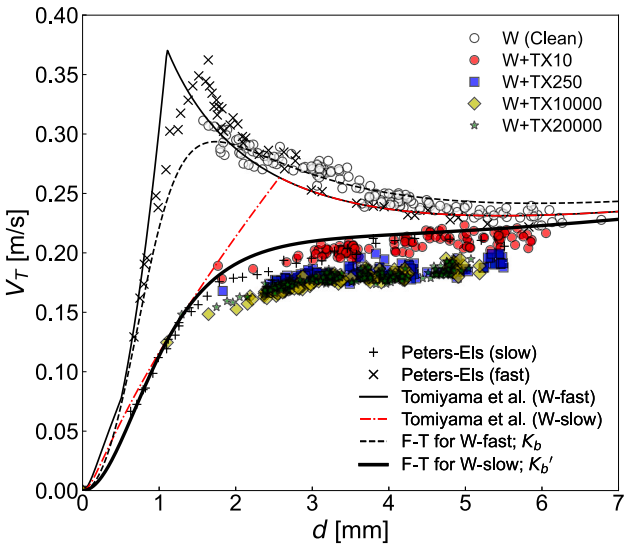

Fig. 10. Bubble terminal velocity in water. W: water, TX: Triton X-100, Tomiyama et al. Eqs. (3) and (5) for fast and slow curves, respectively, in water, F-T: the Fan–Tsuchiya correlation (Eq. (6)) for which K_b (Eq. (9)) with n = 1.6 for fast curve and K_b' (Eq. (10)) with n = 0.8 for slow curve).

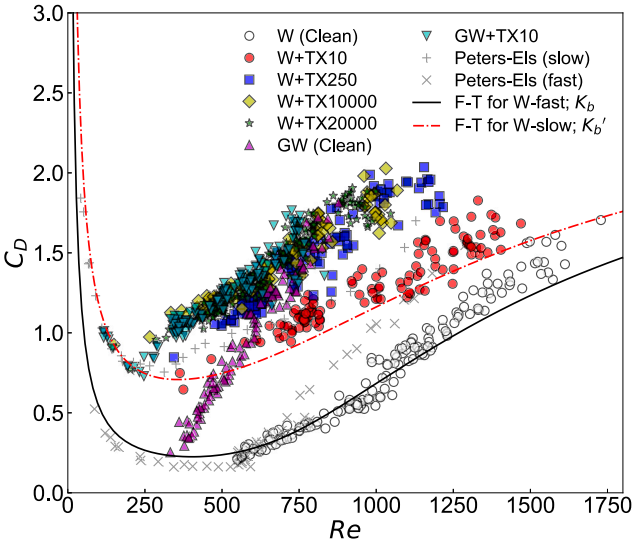

Fig. 11. Drag coefficient. W: water, GW: glycerol solution, TX: Triton X-100, F-T: the Fan–Tsuchiya correlation (Eq. (6)) for fast (Eq. (9) for K_b, n = 1.6) and slow (Eq. (10) for K_b', n = 0.8) curves.

−10.6 slightly larger than the present one (log Mo = −10.8). Bubbles in the contaminated water at 10 mmol/m^3 show a close relationship with the drag curve of the contaminated system in Peters' data, while the data for $C \geq$ 250 mmol/m^3 lie on the upper side of the drag curve of the contaminated system in Peters' data. The drag coefficient increases with increasing the contamination level, while the increasing effect saturates and an upper limit emerges for the significant contamination levels beyond CMC as observed in the terminal velocity. The increase in drag from W+TX10 to W+TX250 implies an extra shape deformation because the surface tension is decreased, and the surfactant effect on deformation would also be saturated at W+TX10000 and W+TX20000; the deformation under contamination will be given in the next section. The difference in the drag curves of $C \geq$ 250 mmol/m^3 and C = 10 mmol/m^3 indicates that the bubbles were in different Morton number systems depending on the level of contamination. This can be seen in

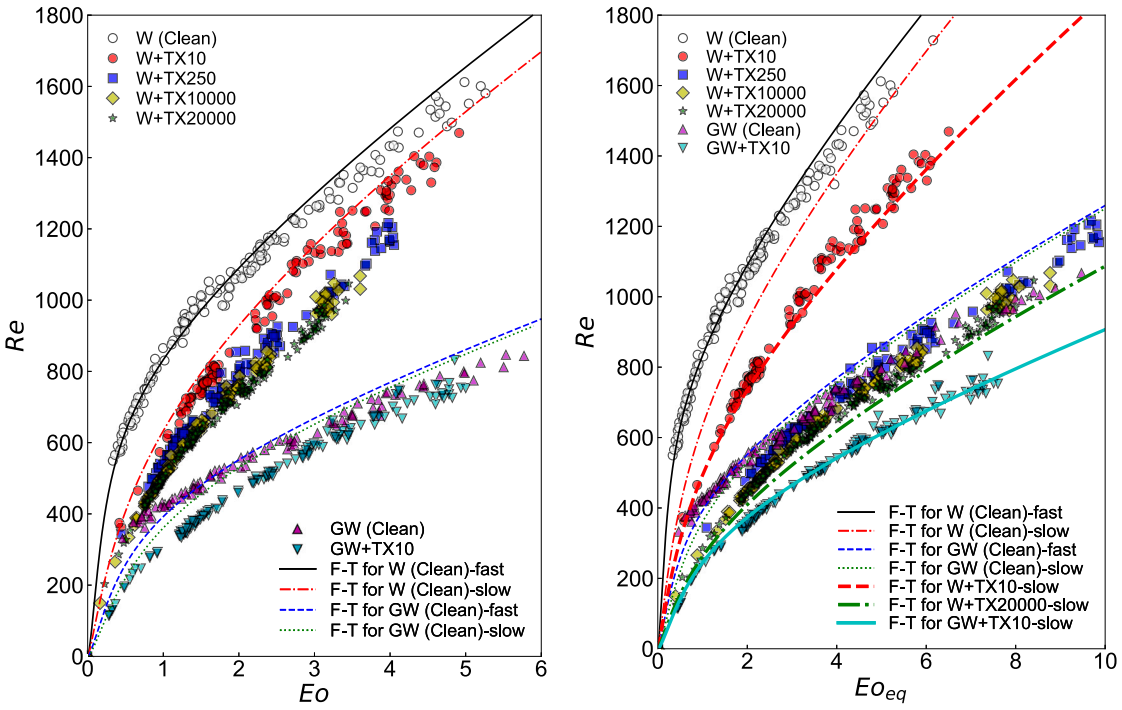

(a) Re-Eo plane (b) Re-Eo_{eq} plane

Fig. 12. Bubble Reynolds number as function of Eo (a) and Eo_{eq} (b). W: water, TX: Triton X-100, GW: glycerol water solution, F-T: the Fan–Tsuchiya correlation (Eq. (6)) for fast (Eq. (9) for K_b, $n = 1.6$) and slow (Eq. (10) for K_b', $n = 0.8$) curves.

the comparison with the glycerol solution data; the data of W+TX10000 and W+TX20000 collapse with those of GW+TX10, which represent slow curve regime of $\log Mo = -9.6$.

To make this point clearer, Re is plotted as a function of Eo in Fig. 12(a). The data of $C = 10$ mmol/m^3 are close to the slow velocity curve given by the Fan–Tsuchiya correlation, but $C = 250$, 10,000 and 20,000 mmol/m^3 show Re lower than it due to the further reduction in velocity. The data of the clean glycerol solution show much lower values due to the higher Morton number ($\log Mo = -9.6$), and those of the contaminated glycerol solution case exhibit a low Re curve for this Morton number, where the Re curves for the glycerol solution cases were drawn using $c = 1.4$ and $n = 1.1$ for a glycerol solution of 53 wt% (Fan and Tsuchiya, 1990) since the coefficients for the present concentration (23 wt%) were not given in the literature. The fact that the Re data exhibit different trends depending on contamination level implies that bubbles behave as they did in a higher Morton number system for reduced surface tension. The lower limit indicated by the collapse of the data of $C = 10{,}000$ and 20,000 mmol/m^3 can be attributed to the saturation of the surface tension reduction at σ_{CMC}. To examine this consideration, Re replotted against the effective Eötvös number, Eo_{eq}, which is based on the surface tension in equilibrium given by Eq. (12), defined by

$$Eo_{eq} = \frac{\Delta\rho g d^2}{\sigma_{eq}} \tag{26}$$

in Fig. 12(b). The contaminated systems of $C = 250$, 10,000 and 20,000 mmol/m^3 clearly show the Re-Eo relationship close to that of the glycerol solution of $\log Mo = -9.6$, and the Re curve of the fully contaminated bubble data on the Re-Eo_{eq} plane agrees with the slow velocity curve of the glycerol solution case on the Re-Eo plane shown in Fig. 12(a). In addition, at $C = 10$ mmol/m^3, the data also agree with the slow velocity curves given by the Fan–Tsuchiya correlation for the corresponding effective Morton numbers $\log Mo_{eq} = -10.4$ and -9.1 in the water and glycerol cases, respectively. Thus, the reduction in surface tension shifts the velocity (drag) curve to the higher-Morton number side. This analysis also supports that σ_{CMC} measured for static surfaces can be used as σ_∞ in Eq. (12) to define the non-dimensional numbers even for interfaces in motion. We will present a drag correlation, which is able to reproduce the surfactant effects via surface tension reduction and shape deformation, in Section 4.5.

4.4. Bubble aspect ratio

Fig. 13 shows the bubble aspect ratio in the clean and contaminated water cases. In all cases, χ increases with increasing d. Some scattering appears in the clean water case, while the variance is mitigated in the contaminated ones. From $C = 0$ to 10 mmol/m^3, the reduction in χ is remarkable. This significant reduction in shape deformation can be mainly attributed to the bubble velocity reduction induced by the Marangoni stress acting on the bubble surface. However, χ increases with an additional increase in the concentration of surfactant. Comparison of the cases of $C = 10{,}000$ and 20,000 mmol/m^3 shows that the change in χ for the surfactant concentration is saturated. This behavior was mentioned in the description for Fig. 6. A similar behavior was observed for V_T in Fig. 10: V_T was significantly reduced at $C = 10$ mmol/m^3, and then further reduction took place at CMC while the change was almost saturated for $C >$ CMC. The increase in χ at $C > 10$ mmol/m^3 suggests a reduction in surface tension due to surfactant adsorption, resulting in the bubble surface exhibiting decreased elasticity and greater deformation.

Fig. 14 compares the aspect ratio data with available correlations expressed in terms of Eo, where the Eötvös number defined for σ_0 is used. The correlations are all given in the following form:

$$\chi = 1 + \alpha Eo^{\beta} \tag{27}$$

The constants α and β are listed in Table 2. The dependence of the experimental data on C is the same as already shown in Fig. 13. The data of the glycerol water solution with Triton X-100 are shown in

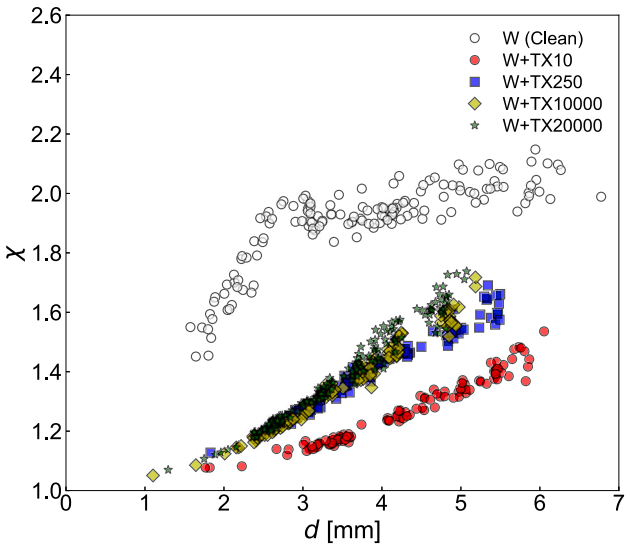

Fig. 13. Bubble aspect ratio in water for different level of contamination. W: water, TX: Triton X-100.

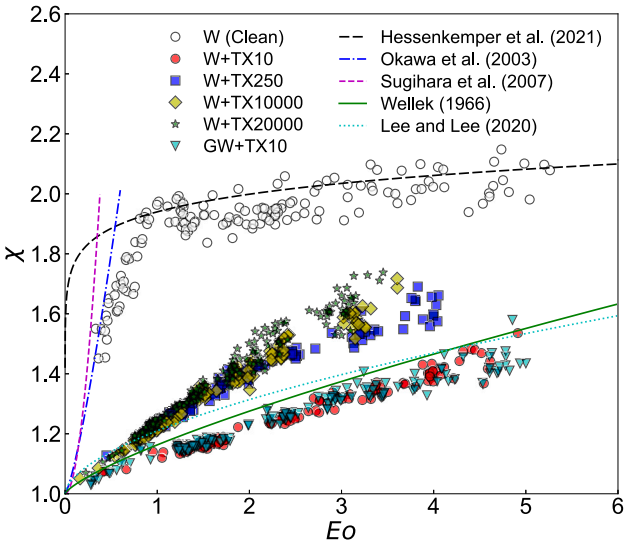

Fig. 14. χ as function of Eo. The correlations are drawn by Eq. (27) with constants given in Table 2.

this figure; the water and glycerol cases with $C = 10$ mmol/m^3 are in good agreement, implying that the Morton number effect on the shape deformation (Legendre et al., 2012) is not notable for the difference in Mo between the two liquids and the contamination brought the reduction in deformation at the same level. The correlation proposed by Hessenkemper et al. (2021) well describes the trend of clean bubbles for $Eo > 1$ although the correlation tends to give an overestimation, except for a large Eo range. The aspect ratio for $Eo < 1$ increases with increasing Eo with a larger increase rate than for $Eo > 1$. The correlations of Okawa et al. (2003) and Sugihara et al. (2007) give a similar trend in this range, but the agreement is not good since those correlations were developed for small bubbles with rectilinear paths. The correlation of Wellek et al. (1966) was proposed for drops in liquids, but it has often been used for contaminated bubbles (Tomiyama et al., 2002). The correlation of Lee and Lee (2020) is similar to the Wellek correlation; Hayashi et al. (2021) pointed out that this fact implies that the filtered water used in their experiments can be considered contaminated. These correlations give reasonable values for

Table 2
Constants in aspect ratio correlations in terms of Eo, Eq. (27).

	α	β	Data
Wellek et al. (1966)	0.163	0.757	Drops in liquids
Okawa et al. (2003)	1.97	1.3	Small bubbles in water
Sugihara et al. (2007)	6.5	1.925	Small bubbles in water
Lee and Lee (2020)	0.21	0.58	Deformed bubbles in water flow
Hessenkemper et al. (2021)	0.94	0.0875	Deformed bubbles in water flow

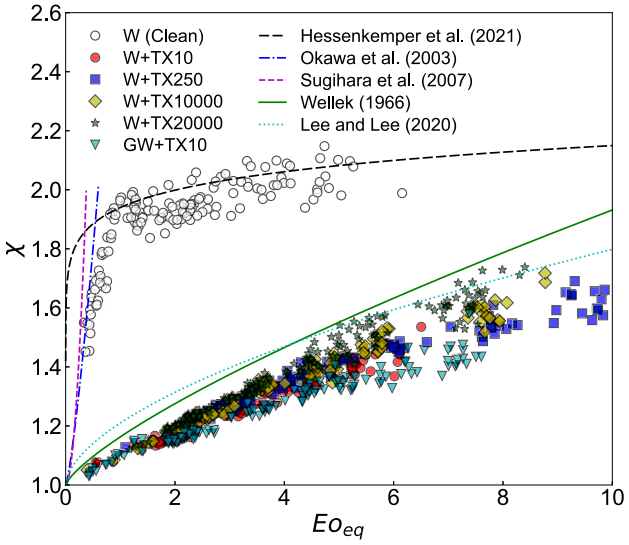

Fig. 15. χ as function of Eo_{eq}. Correlations: Eq. (27) with constants given in Table 2.

the contaminated bubbles of $C = 10$ mmol/m^3, but not for the higher concentration cases.

As we discussed for the Re-Eo_{eq} relation of the contaminated bubbles, the surface tension is modified by contamination and this effect can be considered by using the equilibrium value, σ_{eq}, of the adsorption and desorption in the Eötvös number. Therefore, the data of χ are replotted as a function of Eo_{eq} as shown in Fig. 15. It is clearly demonstrated that the aspect ratio data of the contaminated bubbles collapse onto a single curve although there are some scatter, which could be due to a deviation of the actual surface tension from σ_{eq} due to the presence of fluid flow.

Although the above discussion revealed that Eo_{eq} is more appropriate to correlate the data of contaminated bubbles, the Weber number could be the key dimensionless group related to shape deformation rather than the Eötvös number (Legendre et al., 2012). Fig. 16 shows χ plotted as a function of the Weber number, $We(\sigma_0)$, where the Sugihara et al. (2007) correlation for small bubbles ascending in a straight path through still water and the Legendre correlation for bubbles in liquids of various viscosity are given, respectively, as follows:

$$\chi = 1 + \frac{9}{64}We + \frac{0.04We^2}{\sqrt{3.7 - We}} \tag{28}$$

$$\chi = \left[1 - \frac{9}{64}\left(\frac{We}{1 + 0.2Mo^{0.1}We}\right)\right]^{-1} \tag{29}$$

Hayashi et al. (2021) proposed the following correlation for deformed bubbles in weak-shear flows of water (Hessenkemper et al., 2021) to represent the behavior of χ for $We > 3$:

$$\chi = 1 + 0.62We^{0.376} \tag{30}$$

It would be worth noting that a similar equation was derived from the energy conservation during bubble detachment from a nozzle by Puncochar et al. (2022). Hayashi et al. (2021) proposed to use the following

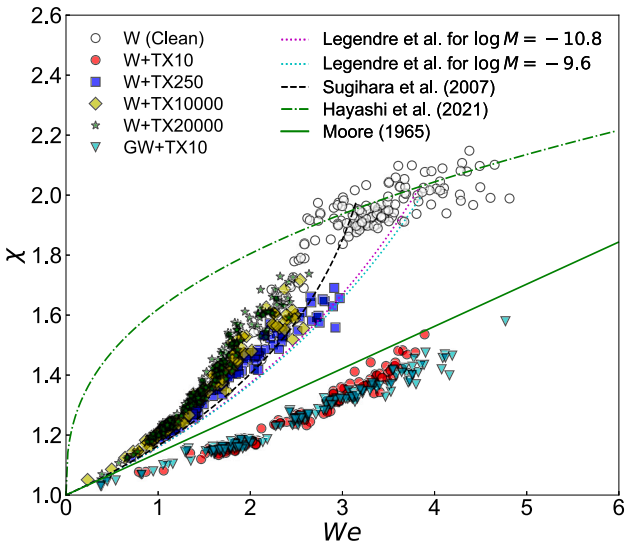

Fig. 16. χ as function of We. Moore: Eq. (32), Sugihara et al.: Eq. (28), Hayashi et al.: Eq. (30), Legendre et al.: Eq. (29).

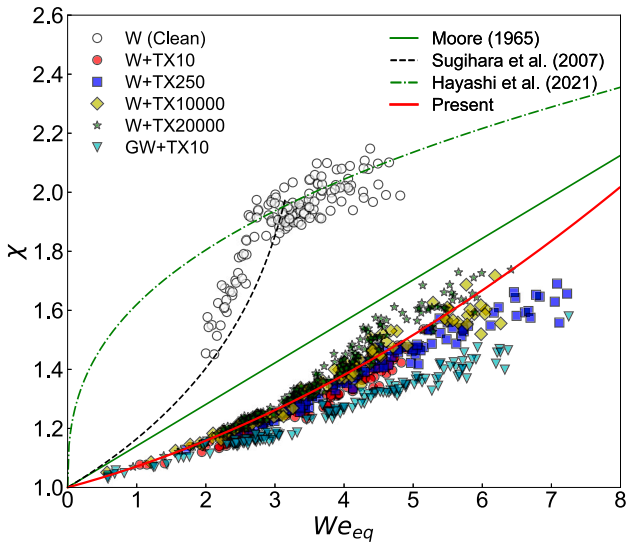

Fig. 17. χ as function of We_{eq}. Moore: Eq. (32), Sugihara et al.: Eq. (28), Hayashi et al.: Eq. (30), Present: Eq. (34).

combination to express the transition of the dependence of χ on We:

$$\chi = \min\left[1 + \frac{9}{64}We + \frac{0.04We^2}{\sqrt{3.7 - We}}, 1 + 0.62We^{0.376}\right] \tag{31}$$

The two equations switch at about $We = 3$. It should however be noted that the Sugihara correlation is for bubbles with rectilinear path. Therefore, the present data of the oscillating bubble for $We < 3$ show values somewhat larger than the Sugihara correlation.

The We value for the transition from spiral to zigzagging mode could be estimated as 2.6 although some bubbles took distorted spiral paths even for $We > 2.6$. The Weber number of 3 mm clean bubble shown in Fig. 5(a) is about 3, so this bubble is in the zigzagging regime. For the path instability that causes the transition from the rectilinear to the oscillating path, Moore (1965) predicted from the balance between the dynamic pressure and the surface tension that the onset of the path instability takes place at $We = 3.745$. Experimentally, Duineveld (1995) and Sugihara et al. (2007) obtained $We = 3.3$ and 3.25, respectively, for the so-called hyper-clean/ultra-pure water. On the other hand, Peters and Els (2012) reported an earlier transition for fast bubbles in tap water, that is, the transition from the rectilinear to the spiral path was observed for $d > 1.5$ mm; Peter's data exhibit an abrupt change in the velocity curve at $d = 1.6$ mm, for which $We = 2.6$. The coincidence of these Weber numbers for the transition from the spiral to the zigzagging and that from the rectilinear to spiral is of interest, and it would be worth investigating the mechanism of the transition in the future.

In spite of the fact that σ_{eq} should be used for the contaminated bubbles, the Weber number defined with σ_0 gives the distribution of the data for high C overlapped with the clean bubble data for $We < 2.5$, and they show a curve similar to the Sugihara and Legendre correlations. This result suggests that if bubbles were fully contaminated we can estimate their aspect ratio using a shape correlation with We by neglecting the reduction in surface tension actually caused in the system. It is not clear whether this is just a coincidence or if there is underlying physics describing the mechanical balance.

Moore (1959) derived the following equation for a bubble slightly deformed from sphere:

$$\chi = 1 + \frac{9}{64}We \tag{32}$$

This model represents the trend of the data of $C = 10$ mmol/m^3; however the data of higher C are largely deviate from the model.

Fig. 17 shows χ plotted as function of the effective Weber number, We_{eq}, defined by

$$We_{eq} = \frac{\rho_L V_T^2 d}{\sigma_{eq}} \tag{33}$$

Except for large We_{eq}, the contaminated water data are well correlated in terms of We_{eq}, supporting again the validity of the use of σ_{eq} for the contaminated bubbles in correlating the bubble dynamics data; not only the bubble Reynolds number (the drag coefficient) but also the shape deformation. Although the Moore model was developed for bubbles slightly deviating from the perfect sphere, the order of χ in the present data is similar to this model. The present data of contaminated bubbles are however smaller than this shape deformation model. This is attributed to the difference in the boundary condition, that is, the surface mobility of the contaminated bubbles deteriorates because of the action of Marangoni stress, while in Moore's theory the potential flow about the sphere is assumed. For the present data of contaminated bubbles, we obtain

$$\chi = \min\left[1 + \frac{We_{eq}}{16} + 0.008We_{eq}^2, \chi_{max}\right] \tag{34}$$

where Eq. (31) can be used for χ_{max} to suppress the value beyond the clean bubble value. The coefficient for the first-order term, 1/16, for contaminated bubbles is smaller than that in Moore's potential flow theory, 9/64. For large deformation range, we need to add the second-order correction term. Thus, the effective Weber number seems a more relevant dimensionless number to the shape deformation, while there are two behaviors intrinsic to the clean and contaminated conditions, which cannot be explained by We_{eq} only and we need the different shape correlations.

The effects of surfactant on the bubble velocity and deformation for the concentration from smaller than to beyond CMC are schematically summarized in Fig. 18. The next section discusses the possibility of modeling the drag increase due to the presence of surfactant through the deformation change.

4.5. Correlating drag coefficients of clean and contaminated data

As discussed in Section 4.2, the velocity correlation proposed by Fan and Tsuchiya (1990) gives a reasonable prediction for the slow velocity curve of contaminated bubbles. However, the coefficients (c and n) in their correlation depend on the liquid phase and are not given

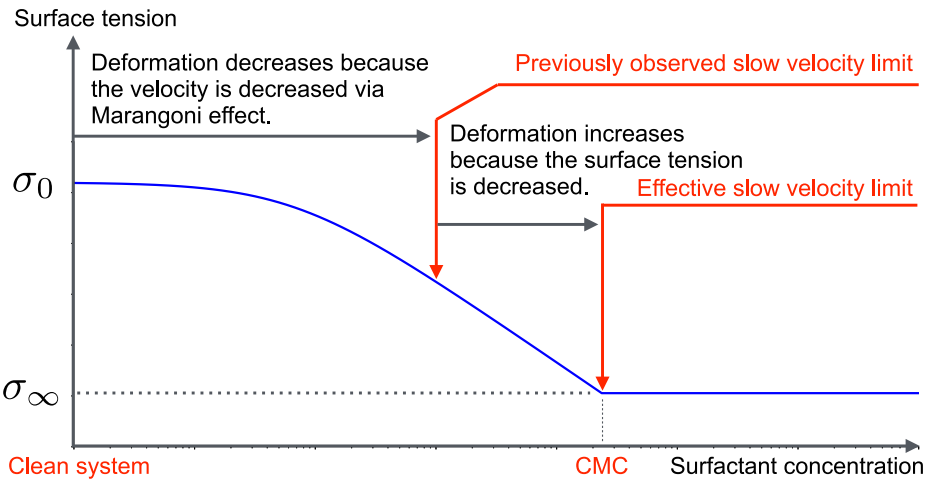

Fig. 18. Surfactant effects on velocity and shape deformation.

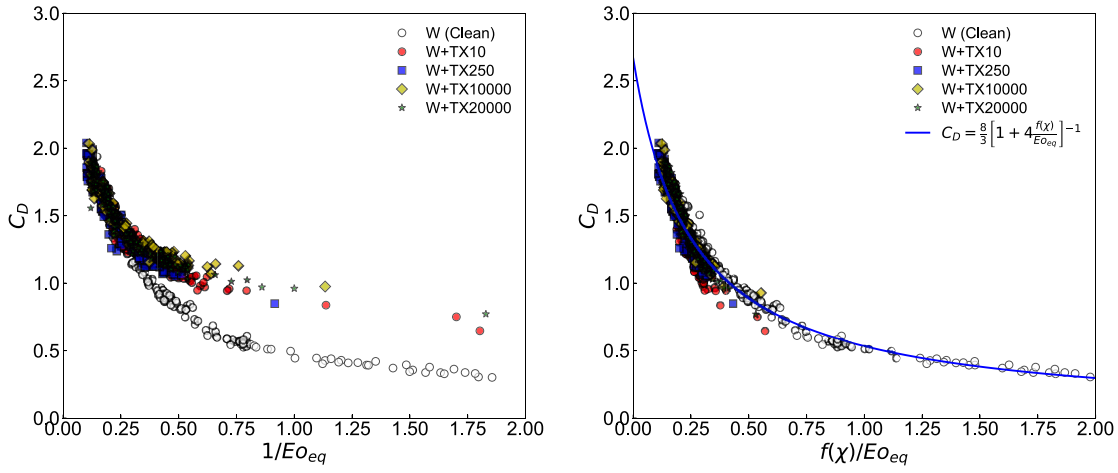

(a) C_D as function of Eo_{eq}^{-1} (b) C_D as function of $f(\chi)Eo_{eq}^{-1}$

Fig. 19. Drag coefficient as function of $f(\chi)/Eo_{eq}$, where $f(\chi) = 2.4(\chi^2 - 1)/\chi^{8/3}$.

as relevant dimensionless groups. By using Eo_{eq} instead of Eo, the Mendelson drag (the function of Eo in Eq. (3)) may be rewritten as

$$C_D = \frac{8}{3}\left[1 + \frac{4}{Eo_{eq}}\right]^{-1} \tag{35}$$

Fig. 19(a) shows C_D plotted as a function of Eo_{eq}^{-1}. For $Eo_{eq}^{-1} > 0.3$, C_D of clean and contaminated bubbles draw different curves, which can be attributed to the different characteristics of bubble shape as observed in Fig. 15. Therefore, the drag correlation should be modified to incorporate the effect of deformation. Tomiyama et al. (2002) demonstrated that, by using their drag model, the effects of surfactant on the rise velocity can be accounted for via the change in bubble shape under the action of the Marangoni stress. On the other hand, the Mendelson drag cannot express the velocity curve for slow bubbles, which has an increasing trend for the bubble diameter, since it does not include any factors for the shape deformation, χ. The velocity-form of the Mendelson drag is given by

$$V_T = \sqrt{\frac{2\sigma}{\rho_L d} + \frac{\Delta\rho g d}{2\rho_L}} \tag{36}$$

In the limiting case of $d \to \infty$ ($Eo \to \infty$) this equation reduces to the well-known equation for spherical-cap bubbles (Clift et al., 1978):

$$V_T = \sqrt{\frac{\Delta\rho g d}{2\rho_L}} \tag{37}$$

corresponding to $C_D \to 8/3$ (Ishii and Chawla, 1979; Clift et al., 1978). Let us therefore introduce a modification only to the surface-tension term to have better fit to the present data so as to keep this limiting value, that is,

$$V_T = \sqrt{\frac{2\sigma_{eq} f(\chi)}{\rho_L d} + \frac{\Delta\rho g d}{2\rho_L}} \tag{38}$$

where $f(\chi)$ is a function of bubble aspect ratio. In the drag form,

$$C_D = \frac{8}{3}\left[1 + \frac{4f(\chi)}{Eo_{eq}}\right]^{-1} \left(= \frac{8}{3}\frac{Eo_{eq}}{Eo_{eq} + 4f(\chi)}\right) \tag{39}$$

This modification assures $C_D \to 8/3$, provided that $f(\chi)/Eo_{eq} \to 0$ as $Eo_{eq} \to \infty$. Note that as Eo_{eq} decreases, the dominant force changes from the surface tension force to the viscous force and the drag is controlled by the Reynolds number in that regime, for which one can use the drag correlations proposed by Chen et al. (2019) as will be

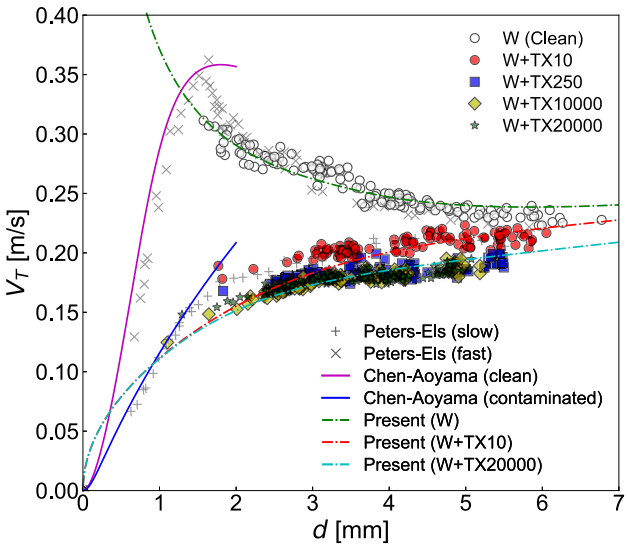

Fig. 20. Bubble terminal velocity in comparison with the new correlation proposed in this work (Eqs. (34) and (39) for C_D and χ, respectively). The fast and slow velocity curves for small bubbles in the viscous force dominant regimes are drawn using the drag correlations proposed by Chen et al. (2019) and the shape correlations proposed by Aoyama et al. (2016) and Aoyama et al. (2018).

shown in Fig. 20. It is important to mention that some studies have also tried to modify this term (Peebles and Garber, 1953; Harmathy, 1960; Fan and Tsuchiya, 1990) (see Eq. (8)); however, they used a constant instead of expressing it as a function of the aspect ratio. Fig. 19(b) shows the C_D data as a function of $f(\chi)/Eo_{eq}$, where the following function is used for $f(\chi)$:

$$f(\chi) = \frac{2.4(\chi^2 - 1)}{\chi^{8/3}} \tag{40}$$

This factor is similar to that appearing in a drag model derived by Tomiyama et al. (2002) based on a potential flow assumption at the bubble nose. The correction factor works well to collapse the clean and contaminated data, and all the data can be reasonably represented by the single curve, Eq. (39).

Fig. 20 shows a comparison between Eq. (39) and the present velocity data in the water cases, where Eqs. (31) and (34) are used for the aspect ratios for the clean and contaminated cases, respectively. The agreement with the data is fairly good, demonstrating that the simple modification of the Mendelson drag introducing the bubble aspect ratio succeeds in reproducing both fast and slow velocity curves of clean and contaminated bubbles, which have different trends in shape. The disagreement for $d < 2$ mm at $C = 10$ mmol/m^3 implies that the significant impact of the Marangoni stress as evident in Fig. 13 makes the bubble surface immobile and the assumption of negligible viscous effect is not sufficiently valid in this regime.

4.6. Discussion on bubble behavior at high surfactant concentrations

The terminal velocities and shapes of bubbles were significantly affected by the presence of surfactant. However, their dependence on the bulk surfactant concentration disappeared at C beyond CMC, and this limit was determined by σ_{CMC}. The contaminated bubbles showed evolutions in V_T and χ different from those of clean bubbles. As shown in Fig. 13, the presence of surfactant greatly mitigates bubble deformation due to the action of Marangoni stress even at C much smaller than CMC (e.g. W+TX10). The Marangoni stress itself does not directly change the deformation, while it requires the liquid side viscous shear to achieve the tangential balance on the bubble surface, which, in turn a smaller interfacial velocity (weaker mobility) is required to produce the viscous shear; therefore, the induced-viscous shear increases the drag. Although the reduction in velocity (dynamic pressure) explains the smaller deformation via the Weber number, the data in the χ-We_{eq} plane exhibit the two distinct curves for the clean and contaminated cases. The contaminated data can be reasonably correlated in terms of We_{eq} regardless of C. This fact supports the notion that the deterioration of surface mobility due to Marangoni stress changes the evolution of bubble deformation. Since the characteristics of the Reynolds number of contaminated bubbles along the slow regime can be understood from the change in the effective Morton number, the Marangoni stress and the effective surface tension characterize the fully contaminated state. However, a slight deviation of the χ data of W+TX10000 and W+TX20000 from the others in the high We_{eq} range implies a second-order contribution of the alteration in surface rheology (Scriven, 1960; Langevin, 2014) for the high concentrations; the surface rheology may change, thus changing the viscous shear and the drag. In the meantime, this change in surface rheology tends to reduce the bubble deformation.

Stebe and Maldarelli (1994) proposed an interesting scenario that the interface mobility of a spherical drop recovers at concentrations higher than CMC since the Marangoni stress no longer plays a role for a uniform concentration distribution formed at the interface fully covered by surfactant. In the present experiment, the surfactant concentration was increased to the very high value (20,000 mmol/m^3 $\gg$ CMC). However, no sign of surface remobilization was observed in the velocity data, that is, the bubbles were in the slow velocity regime of the effective Morton number system. Surface remobilization was reported for small drops in literature (Wang et al., 1999; White and Ward, 2019). Wang et al. (1999) pointed out that the ratio, $(KPe)^{-1}$, of diffusion to advection plays an important role in the remobilization of a rising bubble driven by buoyancy, where K (= Γ_{max}/Cd) is the dimensionless adsorption length (Cuenot et al., 1997) and Pe (= $V_T d/D$) is the Péclet number, and D is the diffusion coefficient. Surface advection sweeps the surfactant to the rear side of a bubble when $(KPe)^{-1} \ll 1$, resulting in a finite concentration gradient throughout the interface, and the Marangoni stress significantly reduces V_T. On the other hand, when $(KPe)^{-1} \gg 1$, the concentration becomes uniform by a large diffusive flux although the total amount of surfactant adsorbed onto the bubble surface increases. The Marangoni stress disappears and the bubble surface is remobilized, which, in turn, V_T regains the value same as in the clean system. This scenario suggests that the bulk concentration required to meet the remobilization condition increases as Pe increases. More recently, White and Ward (2019) carried out experiments on drops in the Stokes regime and reported a similar observation, that is, decreasing the size of the drop caused remobilization because Pe became smaller faster than the Marangoni number, Ma (= $RT\Gamma_{max}/\mu_L V_T$), as the drop size decreased.

For large Reynolds number bubbles, Bel Fdhila and Duineveld (1996) carried out experiments on bubbles in water up to 2 mm diameter. The experiments, in which Triton X-100, Brij$_{30}$ and SDS (sodium dodecyl sulfate) were used as surfactant, showed that V_T became independent of C at concentrations greater than a certain value. The data are however shown only for concentrations much smaller than CMC. Although the behavior of the velocity data around CMC is not discussed in detail, they reported that no remobilization was observed even increasing the concentration of Triton X-100 up to 1000 mmol/m^3, which is four times larger than CMC. No remobilization was attributed to the Biot number, which is the ratio of the desorption rate to the advection rate, smaller than in Stebe's experiment. Wang et al. (1999) pointed out that the reason why the remobilization was not observed in the experiments of Bel Fdhila and Duineveld (1996) is that $(KPe)^{-1}$ was probably much lower than unity. In the present system, $(KPe)^{-1}$ can be estimated as O(10^{-3}) ($\ll 1$) for $d = 4$ mm at the highest concentration, which does not meet the criterion proposed by Wang et al. (1999).

Although the actual Γ at the moving surface is nonuniform, the mean concentration is expected to be close to Γ_{eq} (Hayashi et al., 2025), and $\Gamma_{eq}/\Gamma_{max} = 0.937$ and 0.997 at $C = 10$ and 250 mmol/m^3, respectively, in the present contaminated systems; the latter value is very close to unity, and therefore the bubble surface could be almost entirely covered by surfactant even with a very high Pe estimated 10^6 (Cuenot et al., 1997). However, according to the present result, that concentration is still insufficient to induce surface remobilization. The Marangoni number quantifies how readily the bubble surface can be immobilized due to the Marangoni stress. The surface mobility tends to easily deteriorate in systems with low liquid viscosity because a low-viscosity liquid requires a large velocity gradient at the interface to balance with the Marangoni stress (Hayashi et al., 2025). The Marangoni number evaluated for the typical velocity magnitude 0.23 m/s is $Ma = 35$; The large Marangoni number in the present system implies that surface mobility deteriorates even with a weak gradient in surface tension, which does not result in any signs of surface remobilization. The shape and path oscillations can also be important in preventing remobilization; the surfactant concentration can be nonuniform associated with the oscillations. Interestingly, Basařová et al. (2022) reported surface remobilization of bubbles ($d < 2$ mm) without shape oscillation in aqueous propanol solutions, provided that the propanol concentration is higher than the aggregation concentration. The remobilization was attributed to the fast desorption of propanol from the bubble surface. If the fast desorption is the key to meet the remobilization criteria, this is not a case for Triton X-100 (Takagi and Matsumoto, 2011). More systematic studies are still needed to understand the remobilization criteria in the future.

5. Conclusion

In this study, measurements of the terminal velocities and aspect ratios of single bubbles in contaminated water were carried out to investigate their behavior in the fully contaminated state. Triton X-100, the critical micelle concentration of which is 240 mmol/m^3, was used as surfactant. The bubble diameter ranged from 1 to 6 mm. The surfactant concentration C was 10, 250, 10,000 and 20,000; the latter two are much higher than CMC. The results were compared with the available data and correlations to find a way to correlate the data. The main findings obtained in this study are as follows:

1. The addition of Triton X-100 of $C = 10$ mmol/m^3 induced a significant reduction in terminal velocity, and due to the velocity reduction the deformation was decreased as usually reported in the literature. However, a slower velocity curve was obtained by further increasing the concentration, and the saturation of surfactant effect on the velocity and deformation was clearly observed at C beyond the CMC.
2. The drag curve and the Re-Eo plot made clearer that the contaminated bubbles draw the slow velocity curve as if they were in a higher Morton number system given by the effective surface tension σ_{eq} reduced by surfactant, which increases the Morton and Eötvös numbers of a bubble from the clean system: $(Mo, Eo) \rightarrow (Mo_{eq}, Eo_{eq})$.
3. The aspect ratio of contaminated bubbles was shown as a function of the effective Weber number, We_{eq}, defined with the surface tension at equilibrium of adsorption and desorption, which leads to conclude that the observed behaviors in the drag of contaminated bubbles are resulting from a further increase of deformation because the surface tension is reduced as summarized in Fig. 18.
4. The aspect ratio and drag correlations were proposed by modifying the Moore shape model and the Mendelson drag, respectively, and they were confirmed to give good predictions.

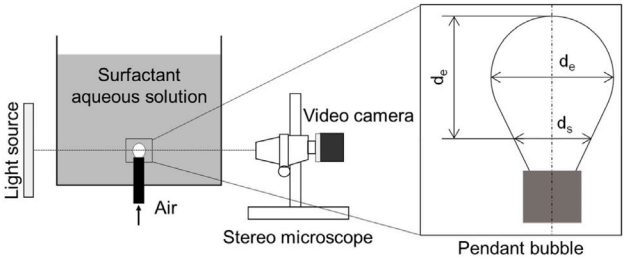

Fig. A.21. Pendant bubble method.

CRediT authorship contribution statement

Yusei Iwai: Writing – original draft, Visualization, Methodology, Investigation, Formal analysis. **Shigeo Hosokawa:** Writing – review & editing, Investigation. **Dominique Legendre:** Writing – original draft, Investigation, Formal analysis, Conceptualization. **Kosuke Hayashi:** Writing – original draft, Visualization, Supervision, Methodology, Investigation, Funding acquisition, Formal analysis, Conceptualization.

Declaration of competing interest

The authors declare that they have no known competing financial interests or personal relationships that could have appeared to influence the work reported in this paper.

Acknowledgments

This research was supported by JSPS KAKENHI 24K00805. KH would like to thank Université Toulouse III Pauls Sabatier and Institut de Mécanique de Fluides de Toulouse for their support to enhance this collaborative research work. The authors also thank Dr. Ryo Kurimoto (Kobe University) for discussion during the experiment.

Appendix A. Pendant bubble method

A schematic of the experimental setup is shown in Fig. A.21. A bubble was generated using a syringe at the tip of the nozzle mounted at the bottom of a small rectangular vessel, and the bubble shape in the steady state was recorded. A high-speed camera (Redlake, Motion Pro HS-1) was used to shoot images. As shown in Fig. A.21, the maximum diameter of the horizontal cross section of the bubble is defined by d_e, and the diameter of the horizontal cross section of the bubble located d_e from the tip of the bubble is denoted as d_s. The surface tension is calculated as

$$\sigma_{eq} = \frac{\Delta\rho g d_e^2}{Q} \tag{A.1}$$

where Q is a function of s $(= d_s/d_e)$. The following equation given by Misak (1968) was used for Q.

$$\frac{1}{Q} = \begin{cases} (0.33/s^{2.57}) - 0.98s^2 + 0.84s - 0.18 & (0.401 \le s \le 0.46) \\ (0.32/s^{2.60}) - 0.47s^2 + 0.50s - 0.13 & (0.46 < s \le 59) \\ (0.32/s^{2.62}) - 0.12s^2 + 0.16s - 0.053 & (0.59 < s \le 0.68) \\ (0.31/s^{2.64}) - 0.092s^2 + 0.15s - 0.059 & (0.68 < s \le 0.9) \\ (0.31/s^{2.85}) - 0.69s^2 + 1.1s - 0.21 & (0.9 < s \le 1.0) \end{cases}$$

The values of surface tension were measured when equilibrium between adsorption and desorption was reached, and the standard errors at 95% confidence interval were less than 2% (Mori et al., 2024).

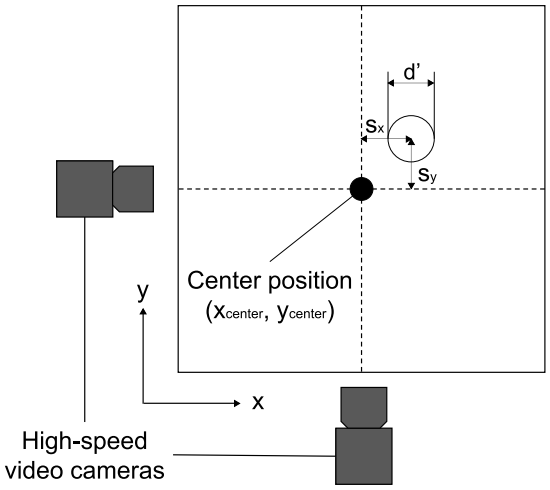

Fig. B.22. Bubble diameter change due to its position.

Appendix B. Scale correction method

The scale factor [mm/pix] was obtained by shooting a stainless steel ruler inserted in the center of the tank. However, the actual length scale changed when a bubble escaped from exactly the center plane due to path oscillation (Fig. B.22). The scale factor was therefore adjusted for the instantaneous bubble position as follows. The change in bubble diameter with relation to the amount of movement from the center plane is calculated as magnification factor, M, per 1 mm as

$$M = \frac{1 - \Delta p}{\Delta s} \tag{B.1}$$

where Δp is the pixel change rate (= backward position pixels/forward position pixels) and Δs is the displacement from center plane (= backward position − forward position). Therefore, the scale transformation, s, in the x and y directions can be calculated by using the distance between the center plane and the bubble position as follows:

$$(s_x, s_y) = (x - x_{center}, y - y_{center}) \tag{B.2}$$

The correction factors in each direction are then given by

$$(\mathrm{CF}_x, \mathrm{CF}_y) = (1 - Ms_x, 1 - Ms_y) \tag{B.3}$$

Thus, the widths of the elliptic disks were adjusted using the correction factors; for example, the bubble volume is given by

$$\vartheta_B = \sum_{j=1}^{N} \frac{\pi L'_{Fj} L'_{Sj} \delta}{4} \tag{B.4}$$

where $(L'_{Fj}, L'_{Sj}) = (\mathrm{CF}_x L_{Fj}, \mathrm{CF}_y L_{Sj})$.

Appendix C. Stress balance analysis

The momentum jump condition in the direction to a bubble surface is given by (Legendre and Zenit, 2025)

$$p_G = p_L - \mathbf{n}_L \cdot \boldsymbol{\tau}_L \cdot \mathbf{n}_L + \sigma\kappa \tag{C.1}$$

where p is the pressure, $\boldsymbol{\tau}$ is the viscous stress tensor, κ is the curvature, $\mathbf{n}$ is the unit outward normal, and the subscripts G and L denote the gas and liquid phases, respectively. The viscous stress in the gas phase is neglected since its magnitude is much smaller than that in the liquid phase. Taking a difference of the jump conditions at the bubble nose (denoted by N) and the bubble equator (denoted by E) yields

$$\delta p_G = \delta p_L - \mathbf{n}_L \cdot \delta\boldsymbol{\tau}_L \cdot \mathbf{n}_L + \sigma\delta\kappa \tag{C.2}$$

where $\delta p = p_k^E - p_k^N$, $\delta\boldsymbol{\tau} = \boldsymbol{\tau}_L^E - \boldsymbol{\tau}_L^N$, and $\delta\kappa = \kappa^E - \kappa^N$. From the Navier–Stokes equation

$$\frac{\nabla p}{\rho} = \mathbf{g} - \mathbf{v} \cdot \nabla\mathbf{v} + \frac{\mu\nabla^2\mathbf{v}}{\rho} \tag{C.3}$$

we evaluate the order-of-magnitude of the pressure gradient by taking the bubble diameter d and the terminal velocity V_T as the length and the velocity scales, respectively, that is,

$$\frac{\delta p_G}{d} \sim \rho_G g - \frac{\rho_G V_T^2}{d} - \mu_G \frac{V_T}{d^2} \tag{C.4}$$

$$\frac{\delta p_L}{d} \sim \rho_L g - \frac{\rho_L V_T^2}{d} - \mu_L \frac{V_T}{d^2} \tag{C.5}$$

Thus,

$$\delta p_G - \delta p_L \sim \rho_L V_T^2 + \mu_L \frac{V_T}{d} - \Delta\rho g d \tag{C.6}$$

where the inertial and viscous terms of the gas phase were omitted. Eliminating the pressure differences in Eq. (C.2) by using the estimated order-of-magnitude, we have

$$c_i \rho_L V_T^2 + c_\mu \mu_L V_T / d - c_b \Delta\rho g d - c_\sigma \sigma / d \sim 0 \tag{C.7}$$

where $\delta\kappa \sim d^{-1}$ and the coefficients c were added to have the equality in the sense of first-order approximation.

Data availability

Data will be made available on request.

References

Aoyama, S., Hayashi, K., Hosokawa, S., Tomiyama, A., 2016. Shapes of ellipsoidal bubbles in infinite stagnant liquids. Int. J. Multiph. Flow 79, 23–30.
Aoyama, S., Hayashi, K., Hosokawa, S., Tomiyama, A., 2018. Shapes of single bubbles in infinite stagnant liquids contaminated with surfactant. Exp. Therm. Fluid Sci. 96, 460–469.
Basařová, P., Crha, J., Pilíková, L., Orvalho, S., 2022. Mutable bubble surface mobility in water – propanol mixtures and its impact on bubble motion and deformation. Chem. Eng. Sci. 260 (117861).
Bel Fdhila, R., Duineveld, P.C., 1996. The effect of surfactant on the rise of a spherical bubble at high Reynolds and Peclet numbers. Phys. Fluids 8 (2), 310–321.
Bonnefis, P., Sierra-Ausin, J., Fabre, D., Magnaudet, J., 2024. Path instability of deformable bubbles rising in Newtonian liquids: a linear study. J. Fluid Mech. 980, A19.
Chang, C.-H., Franses, E.I., 1995. Adsorption dynamics of surfactants at the air/water interface: a critical review of mathematical models, data, and mechanisms. Colloids Surf. A Physicochem. Eng. Aspects 100, 1–45.
Chen, J., Hayashi, K., Hosokawa, S., Tomiyama, A., 2019. Drag correlations of ellipsoidal bubbles in clean and fully contaminated systems. Multiph. Sci. Technol. 31 (3), 215–234.
Clift, R., Grace, J.R., Weber, M.E., 1978. Bubbles, Drops and Particles. Academic Press.
Cuenot, B., Magnaudet, J., Spennato, B., 1997. The effects of slightly soluble surfactants on the flow around a spherical bubble. J. Fluid Mech. 339, 25–53.
Davies, R.M., Taylor, G.I., 1950. The mechanics of large bubbles rising through extended liquids and through liquids in tubes. Proc. R. Soc. Lond. A Math. Phys. Sci. 200 (1062), 375–390.
Duineveld, P.C., 1995. The rise velocity and shape of bubbles in pure water at high Reynolds number. J. Fluid Mech. 292, 325–332.
Fan, L.-S., Tsuchiya, K., 1990. Bubble Wake Dynamics in Liquids and Liquid-Solid Suspensions. Butterworth-Heinemann, Oxford, England.
Frumkin, A., Levich, V.G., 1947. On surfactants and interfacial motion (in Russian). Zh. Fiz. Khim. 21, 1183–1204.
Haberman, W.L., Morton, R.K., 1956. An experimental study of bubbles moving in liquids. Trans. Am. Soc. Civ. Eng..
Hadamard, J.S., 1911. Mouvement permanent tent d'une sphere liquide et visquese dans un liquide visqueux. C. R. Acad. Sci. 152, 1735–1738.
Harmathy, T.Z., 1960. Velocity of large drops and bubbles in media of infinite or restricted extent. AIChE J. 6 (2), 281–288.
Hayashi, K., Hessenkemper, H., Lucas, D., Legendre, D., Tomiyama, A., 2021. Scaling of lift reversal of deformed bubbles in air-water systems. Int. J. Multiph. Flow 142, 103653.
Hayashi, K., Motoki, Y., Legendre, D., Tomiyama, A., 2025. Drag and interfacial vorticity of spherical bubble contaminated with soluble surfactant. Int. J. Multiph. Flow 187, 105173.

Hayashi, K., Tomiyama, A., 2012. Effects of surfactant on terminal velocity of a Taylor bubble in a vertical pipe. Int. J. Multiph. Flow 39, 78–87.
Hayashi, K., Tomiyama, A., 2018. Effects of surfactant on lift coefficients of bubbles in linear shear flows. Int. J. Multiph. Flow 99, 86–93.
Hessenkemper, H., Ziegenhein, T., Rzehak, R., Lucas, D., Tomiyama, A., 2021. Lift force coefficient of ellipsoidal single bubbles in water. Int. J. Multiph. Flow 138, 103587.
Hosen, H.F., Shahmardi, A., Brandt, L., Solsvik, J., 2024. Dynamics of a single bubble in Newtonian and non-Newtonian fluids: Experimental and simulation approaches. Int. J. Multiph. Flow 174 (104789).
Hosoda, S., Abe, S., Hosokawa, S., Tomiyama, A., 2014. Mass transfer from a bubble in a vertical pipe. Int. J. Heat Mass Transfer 69, 215–222.
Hosokawa, S., Masukura, Y., Hayashi, K., Tomiyama, A., 2017. Experimental evaluation of Marangoni stress and surfactant concentration at interface of contaminated single spherical drop using spatiotemporal filter velocimetry. Int. J. Multiph. Flow 97, 157–167.
Igarashi, R., Hachikubo, R., Kurimoto, R., Hayashi, K., 2025. Shapes of surfactant-laden Taylor bubbles in a square microchannel. Microfluid. Nanofluidics 29 (2), 1–13.
Ishii, M., Chawla, T.C., 1979. Local Drag Laws in Dispersed Two-phase Flow. Technical Report ANL-79-105, Argonne National Laboratry.
Kurimoto, R., Hayashi, K., Tomiyama, A., 2013. Terminal velocities of clean and fully-contaminated drops in vertical pipes. Int. J. Multiph. Flow 49, 8–23.
Kushner, L.M., Hubbard, W.D., 1954. Viscometric and turbidimetric measurements of dilute aqueous solutions of a non-ionic detergent. J. Phys. Chem. 58 (12), 1163–1167.
Landel, J.R., Cossu, C., Caulfield, C.P., 2008. Spherical cap bubbles with a toroidal bubbly wake. Phys. Fluids (1994) 20 (12), 122101.
Langevin, D., 2014. Rheology of adsorbed surfactant monolayers at fluid surfaces. Annu. Rev. Fluid Mech. 46 (1), 47–65.
Lee, W., Lee, J.-Y., 2020. Experiment and modeling of lift force acting on single high Reynolds number bubbles rising in linear shear flow. Exp. Therm. Fluid Sci. 115, 110085.
Legendre, D., Zenit, R., 2025. Gas bubble dynamics. Rev. Modern Phys. 97, 025001.
Legendre, D., Zenit, R., Velez-Cordero, J.R., 2012. On the deformation of gas bubbles in liquids. Phys. Fluids 24 (4), 043303.
Levich, V.G., 1962. Physicochemical Hydrodynamics. Prentice Hall.
Magnaudet, J., Mougin, G., 2007. Wake instability of a fixed spheroidal bubble. J. Fluid Mech. 572, 311–337.
Mendelson, H.D., 1967. The prediction of bubble terminal velocities from wave theory. AIChE J. 13 (2), 250–253.
Misak, M.D., 1968. Equations for determining 1/H versus S values in computer calculations of interfacial tension by the pendent drop method. J. Colloid Interface Sci. 27 (1), 141–142.
Moore, D.W., 1959. The rise of a gas bubble in a viscous liquid. J. Fluid Mech. 6 (1), 113–130.
Moore, D.W., 1965. The velocity of rise of distorted gas bubbles in a liquid of small viscosity. J. Fluid Mech. 23 (4), 749–766.
Mori, T., Igarashi, R., Hayashi, K., Kurimoto, R., Tomiyama, A., 2024. Surface coverage ratio of contaminated Taylor bubbles in a square microchannel. Chem. Eng. Res. Des. 204, 343–353.
Okawa, T., Tanaka, T., Kataoka, I., Mori, M., 2003. Temperature effect on single bubble rise characteristics in stagnant distilled water. Int. J. Heat Mass Transfer 46 (5), 903–913.
Olgac, U., Muradoglu, M., 2013. Effects of surfactant on liquid film thickness in the Bretherton problem. Int. J. Multiph. Flow 48, 58–70.
Otsu, N., 1979. A threshold selection method from gray-level histograms. IEEE Trans. Syst. Man Cybern. 9 (1), 62–66.
Palaparthi, R., Papageorgiou, D.T., Maldarelli, C., 2006. Theory and experiments on the stagnant cap regime in the motion of spherical surfactant-laden bubbles. J. Fluid Mech. 559, 1–44.
Pan, R., Green, J., Maldarelli, C., 1998. Theory and experiment on the measurement of kinetic rate constants for surfactant exchange at an Air/Water interface. J. Colloid Interface Sci. 205 (2), 213–230.
Peebles, F.N., Garber, H.J., 1953. Studies on the motion of gas bubbles in liquids. Chem. Eng. Prog. 49 (2), 88–97.
Peters, F., Els, C., 2012. An experimental study on slow and fast bubbles in tap water. Chem. Eng. Sci. 82, 194–199.
Puncochar, M., Ruzicka, M.C., Simcik, M., 2022. Bubble formation and deformation. Chem. Eng. Sci. 260, 117729.
Riboux, G., Risso, F., Legendre, D., 2010. Experimental characterization of the agitation generated by bubbles rising at high Reynolds number. J. Fluid Mech. 643, 509–539.
Ruth, D.J., Aiyer, A.K., Rivière, A., Perrard, S., Deike, L., 2022. Experimental observations and modelling of sub-Hinze bubble production by turbulent bubble break-up. J. Fluid Mech. 951, A32.
Rybczynski, W., 1911. On the translatory of a fluid sphere in a viscous medium. Bull. Acad. Sci. Kracow Ser. A 40–46.
Sadhal, S.S., Johnson, R.E., 1983. Stokes flow past bubbles and drops partially coated with thin films. Part 1. Stagnant cap of surfactant film – exact solution. J. Fluid Mech. 126 (-1), 237–250.
Savic, P., 1953. Circulation and Distortion of Liquid Drops Falling Through a Viscous Medium. Technical Report MT-22, National Research Council of Canada (NRCC).
Schiller, V.L., Naumann, A.Z., 1933. Uber die grundlegenden berechnungen bei der schwerkraftaufbereitung. Zeitschridt Vereines Dtsch. Ingenieure 77, 318–320.
Scriven, L.E., 1960. Dynamics of a fluid interface equation of motion for Newtonian surface fluids. Chem. Eng. Sci. 12 (2), 98–108.
Stebe, K.J., Maldarelli, C., 1994. Remobilizing surfactant retarded fluid particle interfaces: II. controlling the surface mobility at interfaces of solutions containing surface active components. J. Colloid Interface Sci. 163 (1), 177–189.
Sugihara, K., Sanada, T., Shirota, M., Watanabe, M., 2007. Behavior of single rising bubbles in superpurified water (in Japanese). Kagaku-Kogaku Ronbunshu 33, 402–408.
Tagawa, Y., Takagi, S., Matsumoto, Y., 2014. Surfactant effect on path instability of a rising bubble. J. Fluid Mech. 738, 124–142.
Takagi, S., Matsumoto, Y., 2011. Surfactant effects on bubble motion and bubbly flows. Annu. Rev. Fluid Mech. 43 (1), 615–636.
Takagi, S., Ogasawara, T., Matsumoto, Y., 2008. The effects of surfactant on the multiscale structure of bubbly flows. Philos. Trans.: Math. Phys. Eng. Sci. 366 (1873), 2117–2129.
Tomiyama, A., 2004. Drag, lift and virtual mass forces acting on a single bubble. In: 3rd International Symposium on Two-Phase Flow Modelling and Experimentation.
Tomiyama, A., Celata, G.P., Hosokawa, S., Yoshida, S., 2002. Terminal velocity of single bubbles in surface tension force dominant regime. Int. J. Multiph. Flow 28 (9), 1497–1519.
Tomiyama, A., Hayashi, K., 2018. Fundamentals of multiphase flow modeling based on continuum dynamics. In: Encyclopedia of Two-Phase Heat Transfer and Flow III. WORLD SCIENTIFIC, pp. 1–25.
Tomiyama, A., Kataoka, I., Zun, I., Sakaguchi, T., 1998. Drag coefficients of single bubbles under normal and micro gravity conditions. JSME Int. J. Ser. B 41 (2), 472–479.
Wang, Y., Papageorgiou, D.T., Maldarelli, C., 1999. Increased mobility of a surfactant-retarded bubble at high bulk concentrations. J. Fluid Mech. 390 (S0022112099005157), 251–270.
Wellek, R.M., Agrawal, A.K., Skelland, A.H.P., 1966. Shape of liquid drops moving in liquid media. AIChE J. 12 (5), 854–862.
White, A.R., Ward, T., 2019. Surface remobilization of buoyancy-driven surfactant-laden drops at low reynolds and capillary numbers. AIChE J. 65 (1), 294–304.
Wu, M., Gharib, M., 2002. Experimental studies on the shape and path of small air bubbles rising in clean water. Phys. Fluids 14 (7), L49–L52.
Zhang, Y., Finch, J.A., 2001. A note on single bubble motion in surfactant solutions. J. Fluid Mech. 429, 63–66.